# Structural basis for Arf6–MKLP1 complex formation on the Flemming body responsible for cytokinesis

**Hisayoshi Makyio[1,*], Minako Ohgi[2,*], Tomomi Takei[2,*], Senye Takahashi[2], Hiroyuki Takatsu[2,3], Yohei Katoh[2], Ayako Hanai[2], Tomoko Ueda[2], Yasunori Kanaho[4], Yong Xie[5], Hye-Won Shin[2,3], Hironari Kamikubo[6], Mikio Kataoka[6], Masato Kawasaki[1], Ryuichi Kato[1], Soichi Wakatsuki[1,†] and Kazuhisa Nakayama[2,†]**

[1] Structural Biology Research Center, Photon Factory, Institute of Materials Structure Science, High Energy Accelerator Research Organization (KEK), Tsukuba, Ibaraki 305-0801, Japan; [2]Graduate School of Pharmaceutical Sciences and [3] Career-Path Promotion Unit for Young Life Scientists, Kyoto University, Sakyo-ku, Kyoto 606-8501, Japan; [4] Graduate School of Comprehensive Human Sciences and Institute of Basic Medical Sciences, University of Tsukuba, Tsukuba 305–8575, Japan; [5]Institute of Medicinal Plant Development, Chinese Academy of Medical Sciences and Peking Union Medical College, Haidian District, Beijing 100193, China; and [6]Graduate School of Materials Science, Nara Institute of Science and Technology, Ikoma, Nara 630-0192, Japan

[*]These three authors contributed equally to this work.

[†]Correspondence to: S. Wakatsuki (soichi.wakatsuki@kek.jp) or K. Nakayama (kazunaka@pharm.kyoto-u.ac.jp)

Running title: Role of the Arf6–MKLP1 complex in cytokinesis

**A small GTPase, Arf6, is involved in cytokinesis by localizing to the Flemming body (the midbody). However, it remains unknown how Arf6 contributes to cytokinesis. Here we demonstrate that Arf6 directly interacts with mitotic kinesin-like protein 1 (MKLP1), a Flemming body–localizing protein essential for cytokinesis. The crystal structure of the Arf6–MKLP1 complex reveals that MKLP1 forms a homodimer flanked by two Arf6 molecules, forming a 2:2 heterotetramer containing an extended β-sheet composed of 22 β-strands that spans the entire heterotetramer, suitable for interaction with a concave membrane surface at the cleavage furrow. We show that, during cytokinesis, Arf6 is first accumulated around the cleavage furrow and, prior to abscission, recruited onto the Flemming body via interaction with MKLP1. We also show by structure-based mutagenesis and siRNA-mediated knockdowns that the complex formation is required for completion of cytokinesis. A model based on these results suggests that the Arf6–MKLP1 complex plays a crucial role in cytokinesis by connecting the microtubule bundle and membranes at the cleavage plane.**

Cytokinesis is the final stage of cell division, during which cells exhibit drastic morphological changes and remodeling of the cytoskeleton (Balasubramanian et al, 2004; Glotzer, 2005). In anaphase/telophase, an actomyosin contractile ring constricts the plasma membrane in the equatorial region of a dividing cell to form a cleavage furrow, while an overlapping region of antiparallel microtubules from the central spindle gradually forms a dense structure, the Flemming body, in the middle of the intercellular bridge (Note that, although this dense structure is often referred to as the midbody, we hereafter refer to it as the Flemming body to avoid confusion between the terms 'midbody', the entire central spindle, and midbody microtubules). Finally, the cell undergoes abscission on either side of the Flemming body to generate two daughter cells. The drastic shape changes and membrane fission event during cytokinesis entail local delivery and/or removal of membranes and specific proteins (Prekeris & Gould, 2008; Steigemann & Gerlich, 2009). For example, proteins involved in membrane tethering, fusion and fission, such as exocyst components, SNARE proteins and ESCRT subunits, accumulate around the intercellular bridge and the Flemming body (Neto et al, 2011; Prekeris & Gould, 2008). Furthermore, coordination of changes in the organization of membranes and cytoskeleton suggests that interactions occur between components of the membrane trafficking and cytoskeleton remodeling machineries.

Members of the Arf (ADP-ribosylation factor) family of small GTPases regulate various aspects of membrane traffic. Mammals have six Arf isoforms, which are divided into three classes based on sequence similarity (Kahn et al, 2006): class I, Arf1–Arf3 (humans lack Arf2); class II, Arf4 and Arf5; and class III, Arf6. Arf6 is divergent from Arf1–Arf5, and localizes to the plasma membrane and the endocytic system, where it regulates endosome recycling and remodeling of actin and membranes (D'Souza-Schorey & Chavrier, 2006). In addition to these roles in interphase cells, Arf6 has been suggested to be required for the final phase of cytokinesis in mammalian cells (Schweitzer & D'Souza-Schorey, 2002; Schweitzer & D'Souza-Schorey, 2005). Furthermore, a *Drosophila arf6* mutant exhibits male sterility due to a cytokinesis defect during spermatocyte meiosis, although somatic cell mitosis appears to be normal (Dyer et al, 2007).

During cytokinesis, Arf6 transiently localizes to the Flemming body; however, the molecular mechanism underlying its targeting remains controversial. The roles of FIP3 and FIP4 (Rab11 family–interacting protein 3 and 4), which are dual effectors of Rab11 and Arf6 and associate with recycling

endosomes in interphase cells, are the subject of debate. One previous study suggested that Arf6 is recruited to the Flemming body independently of Rab11- and FIP3-containing endosomes (Fielding et al, 2005), whereas other studies have proposed that Arf6 requires an interaction with Rab11- and FIP3-positive endosomes to be targeted to the cleavage furrow (Montagnac et al, 2009; Schonteich et al, 2007).

In the course of our previous study on the roles of Rab11 and Arf6 in the localization of FIP3 during cytokinesis, we obtained evidence indicating that Arf6 is recruited onto the Flemming body independently of Rab11 and FIP3 (Takahashi et al, 2011). In this study, we extend these observations to show that Arf6 targeting to the Flemming body depends on its direct binding to MKLP1 (mitotic kinesin-like protein 1; also known as KIF23), which together with MgcRacGAP/Cyk4 constitutes the centralspindlin complex at the Flemming body (Balasubramanian et al, 2004; Glotzer, 2005). We have determined the crystal structure of a complex between the MKLP1 C-terminal domain and Arf6, revealing a unique extended β-sheet of 22 strands that spans the entire 2:2 Arf6–MKLP1 complex. This interaction of MKLP1 with Arf6 is unique among Arf–effector interactions. Structure-based mutagenesis and siRNA-mediated knockdowns allowed us to critically test models of Arf6 recruitment to the Flemming body. Our findings demonstrate that formation of the Arf6–MKLP1 complex is crucial for faithful completion of cytokinesis.

## RESULTS

### *Specific association of GTP-bound Arf6 to the Flemming body*

As a first step toward characterizing the specific localization of Arf6 to the Flemming body, we examined the localization of Arf proteins during cytokinesis in HeLa cells (Figure 1A, B). C-terminally mCherry-tagged Arf6 exhibited a distinct localization to the Flemming body in a late phase of cytokinesis, whereas no such Flemming body localization of other Arf proteins examined (Arf1, Arf3 and Arf5) was evident. At high levels of expression of Arf1-mCherry, however, a weak signal could be seen at the Flemming body. We next asked whether the activation status of Arf6 was critical for localization at the Flemming body. In order to address this issue, we took advantage of the dominant activating and inactivating mutants, respectively, Arf6(Q67L) and Arf6(T27N) (Figure 1C, D). Both the wild type (top

row) and activated Arf6 mutant (middle row) localized to the Flemming body. In contrast, Arf6(T27N), which is a nucleotide-free form (Macia et al, 2004), exhibited little or no staining at the Flemming body (bottom row).

We next examined spatiotemporal changes in the localization of Arf6 during mitosis, using three-dimensional time-lapse imaging to follow Arf6-EGFP expressed in HeLa cells (Figure 1E and Movie S1). In metaphase, when the cells were nearly spherical, Arf6-EGFP was uniformly distributed throughout the cytoplasm (Figure 1E, top panels (0:00), the dividing cell marked by a yellow asterisk). At the onset of cytokinesis, Arf6-EGFP transiently accumulated at the ingressing cleavage furrow (0:35, cyan arrow). Three-dimensional image analysis of fixed cells suggested that Arf6-EGFP is localized in the cortical region of the cleavage plane but not on the central spindle (Movie S2). Arf6-EGFP then became increasingly concentrated at the Flemming body as cytokinesis proceeded (Figure 1E, green arrows). Upon abscission, Arf6-EGFP was incorporated into one of the daughter cells as a Flemming body remnant (3:40, red arrows in the cell with a magenta asterisk; 6:00, in the cell with a yellow asterisk). Intriguingly, the Flemming body remnant subsequently crawled up along the cortical surface of the daughter cell (4:30 and 6:00, red arrows in the cells with magenta asterisks) (see Discussion).

***Phenotype of Arf6-knockout cells***

Two different laboratories have published studies using Arf6 siRNAs, but their experiments yielded contradictory results: one study showed that Arf6-knockdown cells exhibited a two-fold increase in the percentage of binucleate cells (Schweitzer & D'Souza-Schorey, 2005), whereas the other study showed that a similar siRNA treatment did not change the number of binucleate cells (Yu et al, 2007). To circumvent problems inherent to the siRNA approach (*i.e.*, incomplete protein depletion and off-target effects), we exploited mouse embryonic fibroblasts (MEFs) established from an Arf6-knockout (KO) mouse (Suzuki et al, 2006) to evaluate the role of Arf6 in cytokinesis. As shown in Figure 1F, multinucleate cells (cells with ≥3 nuclei) were observed in a fraction of Arf6-KO MEFs. Counting the numbers of both binucleate and multinucleate cells revealed that, as compared with wild-type MEFs, Arf6-KO MEFs frequently exhibited a multinucleate phenotype indicative of failed cytokinesis (Figure 1G); note that, the percentage of multinucleate cells might be underestimated because cytokinesis failure potentially reduces cell viability.

Taken together, these data indicate that Arf6 contributes to cytokinesis.

***Characterization of the Arf6–MKLP1 interaction***

Approximately a dozen years ago, Boman *et al.* reported that Arf isoforms interacted with MKLP1 in the yeast two-hybrid system (Boman et al, 1999). MKLP1 constitutes the centralspindlin complex together with MgcRacGAP/Cyk4 and plays an essential role in cytokinesis by localizing to the Flemming body (Glotzer, 2005; Matuliene & Kuriyama, 2002; Mishima et al, 2002). However, the physiological relevance of this interaction has never been clearly established. Given the Flemming body localization of Arf6, its direct binding to MKLP1, and the role of MKLP1 in the centralspindlin complex, we set out to reevaluate the functional implications of the Arf6–MKLP1 interaction.

In humans, there are two splice variants of MKLP1 (Figure 2A); a longer form of 960 amino acids, and a shorter form of 856 amino acids that lacks residues 690–793 of the longer one. We used the shorter form in the following experiments because our preliminary experiments indicated that it is predominant in HeLa cells; the region missing in the shorter form is dispensable for the MKLP1 interaction with Arf6 (see below); and each form localizes to the Flemming body. Hereafter, residue numbering corresponds to the sequence of the shorter form.

We found that a region near the C-terminus of MKLP1 was necessary and sufficient for binding to Arf6; residues 690–807 of MKLP1 are required for binding to Arf6(Q67L), as the 118-residue region fused to GST was sufficient to specifically pull down Arf6(Q67L)-HA from solution. C-terminal truncation of this domain by only 18 residues (MKLP1(690–789)) abolished the ability to pull down Arf6(Q67L)-HA, suggesting a particularly important role for the C-terminal peptide region (Figure 2B). This result was unexpected, because Boman *et al.* (1999) reported that the region of MKLP1 C-terminal to residue 720 was dispensable for the interaction with Arf proteins in yeast two-hybrid assays (discussed below). The Arf-binding domain of MKLP1 (residues 690–807; hereafter referred to as cMKLP1) was sufficient to pull down wild-type Arf6 or Arf6(Q67L), but not Arf6(T27N) (Figure 2C). This domain also interacted with all Arf isoforms examined (Arf1, Arf3, Arf5 and Arf6) when they were expressed in HeLa cells as constitutively activated proteins (Figure 2D). In addition, surface plasmon resonance (SPR) measurements revealed that cMKLP1 showed the highest affinity to Arf6 (with a $K_d$ value of 16 μM) among the Arf

isoforms examined (Figure 2E); the $K_d$ values of Arf1, Arf3 and Arf5 were 120, 87 and 120 μM, respectively.

***Characterization of Arf6 and MKLP1 on the Flemming body***

Next, we compared the localization of endogenous Arf6 and MKLP1 by immunofluorescence analysis. In the majority of cells during cytokinesis, Arf6 and MKLP1 were colocalized at the Flemming body (Figure 3A, lower row). However, some cells exhibited MKLP1, but not Arf6, on the Flemming body (upper row). After closer examination of this variability in results, we noted a strong correlation between the presence of a relatively thick central spindle, suggestive of an earlier phase of cytokinesis, and the absence of Arf6 colocalization with MKLP1 at the Flemming body (Figure 3A, upper row, and Figure 3B). In contrast, cells with a relatively thin central spindle, indicating a later phase of cytokinesis, exhibited colocalization of MKLP1 and Arf6 (Figure 3A, lower row, and Figure 3B). These observations reveal a clear temporal distinction between the times at which MKLP1 and Arf6 are recruited to the Flemming body, and suggest that Arf6 may be recruited to the Flemming body through its binding to MKLP1.

To begin to test this model, we next performed time-lapse analysis of cells co-expressing Arf6-EGFP and mRFP-MKLP1. As shown in Figure 3C and Movie S3, mRFP-MKLP1 appeared first on the Flemming body (for example, see 0:10). After that time point, Arf6-EGFP started accumulating around the ingressing cleavage furrow (0:15 and 0:20). As cytokinesis proceeded, Arf6-EGFP became colocalized with mRFP-MKLP1 on the Flemming body (0:30–1:10). After abscission, Arf6-EGFP and mRFP-MKLP1 were incorporated *en bloc* into one of the daughter cells as a Flemming body remnant (2:00 and 3:00). The time-lapse data indicate that the localization of MKLP1 to the Flemming body is independent of Arf6. To confirm this, we examined the localization of MKLP1 in Arf6-KO MEFs (Figure 3D). MKLP1 was found on the Flemming body in Arf6-KO MEFs (lower row), as in wild-type MEFs (upper row), confirming Arf6-independent localization of MKLP1 to the Flemming body.

***Overall structure of the Arf6–MKLP1 complex***

To elucidate the molecular basis for the GTP-dependent interaction of Arf6 with MKLP1, we determined the crystal structure at 3.0 Å resolution of an N-terminal truncation of Arf6(Q67L) (residues 13–175; referred to as Arf6 in the context of X-ray crystallography and small angle X-ray scattering (SAXS)

measurements) in complex with cMKLP1. The crystals of the Arf6–cMKLP1 complex belonged to the space group $P2_1$, and its overall structure is shown in Figure 4A. The asymmetric unit contains four Arf6–cMKLP1 complexes, which are similar to one another: Cα-atom root-mean-square deviations (RMSD) of four Arf6 (Arg15–Asn172)–cMKLP1 (Arg714–Pro799) complexes were between 0.21 Å and 0.42 Å. The cMKLP1 structure is composed of five strands (β1: Trp715–His718, β2: Ala737–Val740, β3: Lys753–Leu761, β4: Ile767–Lys778, β5: Gln784–Lys795), one short helix (α1: Glu745–Lys750), and a long loop (Pro720–Val734) including the short βA region (Val729–His733) (Figure S1A), which is assigned to constitute a small β sheet in the cMKLP1 homodimer (Figure 4A, B). In the crystal, two cMKLP1 molecules form a homodimeric core held together by two layers of anti-parallel β-strand interactions, the major interaction between two β5-strands and the minor one between two βA-strands of cMKLP1 (Figure 4B). The two Arf6 molecules flank the cMKLP1 homodimer on either side, and do not make direct contact with each other. The overall heterotetramer is a rectangular parallelepiped with approximate dimensions of 51 Å × 54 Å × 96 Å (Figure 4A). One striking feature of the 2:2 Arf6–cMKLP1 heterotetrameric complex is an extended β-sheet of 22 β-strands that spans the entire complex (Figure 4B, a shadowed region). The buried surface areas between Arf6 and cMKLP1, and between cMKLP1 and cMKLP1, are respectively 2241 $Å^2$ (surface complementarity Sc values: 0.69) and 2080 $Å^2$ (Sc values: 0.78) (Table S1).

SAXS measurements were carried out in order to detect the formation of the Arf6–cMKLP1 heterotetramer in solution (Figure 4C). Guinier analysis revealed that the molecular size of the Arf6–cMKLP1 complex changes as a function of its concentration: at higher concentrations, size increased gradually and eventually reached that of the heterotetramer. We also confirmed formation of the cMKLP1 dimer in solution by chemical cross-linking experiments (Figure S2), indicating that the heterotetramer in the crystal reflects a form that occurs naturally in solution, rather than a crystallographic artifact. Statistics regarding the structure determination and its refinement are summarized in Table S2. Multiple alignment, secondary structure and binding sites of the solved Arf6 and cMKLP1 structures are summarized in Figure S1. Unless otherwise noted, we hereafter describe the structural details using chain A (Arf6) and chain B (cMKLP1) in the crystal.

***Interactions between Arf6 and cMKLP1***

The interface between Arf6 and cMKLP1 in the complex (Figure 5A-C) effectively explains the GTP-dependence of the interaction between the two proteins (Figure 2C) (Boman et al, 1999). The GDP–GTP cycle of Arf6 results in significant conformational changes in the switch 1 (Sw1) and switch 2 (Sw2) regions, as well as an additional interswitch toggle that causes a two-residue register shift (Pasqualato et al, 2001). In the GDP-bound state, the Sw1 region retracts, resulting in formation of a new β-strand (β2') (Figure 5C) (Ménétrey et al, 2000; Pasqualato et al, 2001; Pasqualato et al, 2002). In the complex between GTP-bound Arf6 and MKLP1, the β2'-strand overlaps with the β5-strand of MKLP1 (Figure 5C), thus interfering with the $\beta2^{Arf6}$–$\beta5^{MKLP1}$ inter-strand interaction.

Although the hydrophobic residues of Arf6 involved in the Arf6–cMKLP1 interaction are similar to those playing analogous roles in the Arf6–CTA1 and Arf6–JIP4-LZII complexes (Figure S1) (Isabet et al, 2009; O'Neal et al, 2005), a search of the Dali server (Holm & Rosenström, 2010) revealed no structures similar to that of cMKLP1. The unique structure of cMKLP1 allows hydrogen bond interactions between residues in the hydrophobic pocket and $Phe47^{Arf6}$, $Trp62^{Arf6}$ and $Tyr77^{Arf6}$ (Figure 5D); these residues are conserved in the Arf and Rab GTPase families and are collectively called a 'triad patch' (Chavrier & Ménétrey, 2010; Kawasaki et al, 2005; Ménétrey et al, 2007; Merithew et al, 2001). First, $\beta2^{Arf6}$ and $\beta5^{cMKLP1}$ make an anti-parallel inter-protein β-sheet interaction (Figure 5D, E). $Val45^{Arf6}$, $Phe47^{Arf6}$ and $Val49^{Arf6}$ make main-chain hydrogen bonds with $Phe788^{cMKLP1}$, $Val786^{cMKLP1}$ and $Gln784^{cMKLP1}$, respectively. There are also two side-chain hydrogen bonds ($Asn48^{Arf6}$-$Ser785^{cMKLP1}$ and $Glu50^{Arf6}$-$Thr779^{cMKLP1}$) on this interface. Second, $His758^{cMKLP1}$ makes a hydrogen bond to $His76^{Arf6}$ in the GTP-sensitive Sw2 (Figure 5F). In this region, the hydrophobic interface includes $Leu73^{Arf6}$ and $His76^{Arf6}$ along with $Pro720^{cMKLP1}$, $Leu756^{cMKLP1}$, $His758^{cMKLP1}$ and $Ile772^{cMKLP1}$. $His758^{cMKLP1}$ interacts with both $Leu73^{Arf6}$ and $His76^{Arf6}$. A third interface is present at the triad patch formed by $Phe47^{Arf6}$, $Trp62^{Arf6}$, and $Tyr77^{Arf6}$. $Ala743^{cMKLP1}$, $Tyr754^{cMKLP1}$ and $Val786^{cMKLP1}$ are involved in the interaction with the triad patch, with $Phe47^{Arf6}$ and $Tyr77^{Arf6}$ forming three hydrogen bonds with $Val786^{cMKLP1}$ and $Tyr754^{cMKLP1}$, respectively (Figure 5G). $Trp62^{Arf6}$ does not engage in hydrogen bond interactions with the residues of effector proteins such as cMKLP1 and CTA1, with the exception of JIP4-LZII. $Phe788^{cMKLP1}$ is located

between the Sw1 and Sw2 regions, and its main chain forms a hydrogen bond with that of Val45$^{Arf6}$ (Figure 5D, E, G). The position of the Phe788$^{cMKLP1}$ residue is conserved not only in various Arf effectors but also in Rab effectors (Kawasaki et al, 2005).

***Arf6–MKLP1 interaction is required for Arf6 localization to the Flemming body and for cytokinesis***

Based on the crystal structure, we introduced mutations into Arf6 and MKLP1 that were designed to perturb the Arf6–MKLP1 interaction. We focused on the hydrophilic interactions between His76$^{Arf6}$ and His758$^{MKLP1}$ and between Tyr77$^{Arf6}$ and Tyr754$^{MKLP1}$, because our previous structural study of Arf1 in complex with the GGA1-GAT domain revealed that the corresponding His and Tyr residues of Arf1 are critical for this interaction (Shiba et al, 2003). When assayed by pull down with GST-GGA1, GST-JIP4 or GST-FIP4 (Figure 6A), both H76A and Y77A mutations in Arf6(Q67L) abolished the interaction with the GST-fusion proteins. The Y77A mutation also abolished Arf6 binding to MKLP1, when assayed by pulldown with GST-cMKLP1 (Figure 6A). However, Arf6(H76A) retained binding to cMKLP1 in the same assay (Figure 6A). When the Y754A or H758A mutation was introduced into cMKLP1, only the former mutation substantially reduced the binding to Arf6 (Figure 6B). These results highlight the conclusion that the interaction between Tyr77$^{Arf6}$ and Tyr754$^{MKLP1}$ is critical to formation of the complex, while that between His76$^{Arf6}$ and His758$^{MKLP1}$ is dispensable (see Discussion).

We then used the Arf6 and MKLP1 mutants to test whether the Arf6–MKLP1 interaction is crucial for targeting of Arf6 to the Flemming body (Figure 6C, D). When expressed in HeLa cells, Arf6-EGFP (Figure 6C, top row) and the MKLP1 binding–competent Arf6(H76A)-EGFP (middle row) both localized to the Flemming body, like endogenous Arf6. In contrast, the MKLP1 binding–defective Arf6(Y77A) mutant was unable to localize to the Flemming body (bottom row).

We also exploited MKLP1 mutants to determine whether MKLP1 is responsible for recruiting Arf6 to the Flemming body, and whether the loss of Arf6 recruitment is associated with any defects in cytokinesis. We first knocked down endogenous MKLP1 in HeLa cells using siRNAs, and examined the localization of Arf6. A number of control cells exhibited immunostaining for both MKLP1 and Arf6 on the Flemming body or its remnant (Figure 6E, upper panels; green for MKLP1, red for Arf6). Because MKLP1 is essential for Flemming body formation and completion of cytokinesis (Zhu et al, 2005), knockdown of MKLP1

abolished not only the MKLP1 signals but also the Arf6 signals on the Flemming body and its remnants, and increased the population of multinucleate cells (Figure 6E, lower panels, and Figure 6H). We determined whether exogenous expression of MKLP1 mutants restored the Flemming body localization of endogenous Arf6 in the context of MKLP1 knockdown (Figure 6F, G). Like wild-type MKLP1 (Figure 6F, top row), the Arf6 binding-competent MKLP1(H758A) mutant (bottom row) localized to the Flemming body where it was able to recruit Arf6. In contrast, the Arf6 binding-defective mutant, MKLP1(Y754A) (middle row), could not restore the Flemming body localization of Arf6, even though this mutant itself localized to the Flemming body and was able to recruit MgcRacGAP/Cyk4 to the Flemming body like wild-type MKLP1 (Figure S3). In the rescue experiment, we counted the numbers of bi- and multinucleate cells. Co-transfection of the wild-type MKLP1 or MKLP1(H758A) vector together with the MKLP1 siRNAs significantly decreased the percentage of multinucleate cells (Figure 6H). In contrast, co-transfection of the MKLP1(Y754A) vector led to a marginal, if any, rescue of the multinucleate phenotype. These observations demonstrate that Arf6 must bind to MKLP1 in order to be recruited to the Flemming body. Furthermore, loss of Arf6 recruitment diminishes the ability to faithfully complete cytokinesis and is correlated with an increase in polyploidy.

## DISCUSSION

In this study, we have shown that Arf6 is recruited onto the Flemming body by interacting with MKLP1 prior to abscission during cytokinesis. We have also revealed the molecular basis for the Arf6–MKLP1 interaction, and demonstrated that Arf6 and MKLP1 form a 2:2 heterotetramer containing a unique β-sheet composed of 22 strands that spans the entire heterotetramer. Furthermore, using mutants of Arf6 and MKLP1 designed on the basis of the crystal structure, we have confirmed that the Arf6–MKLP1 interaction is crucial for proper cytokinesis.

### *Targeting of Arf6 to the MKLP1-positive Flemming body and its implication in cytokinesis*

We have shown that Arf6 targeting to the Flemming body requires its interaction with MKLP1. Arf6 appears first to be concentrated around the ingressing cleavage furrow (Figure 1E, cyan arrow, and Movies S1 and S2), and is subsequently recruited onto the Flemming body, where MKLP1 has been

previously localized (Figure 3C and Movie S3). Together with experiments using Arf6-KO MEFs (Figure 3D) and MKLP1 siRNAs (Figure 6E, F), these observations support a model in which Arf6 targeting to the Flemming body depends on MKLP1.

MKLP1 is required for formation of the Flemming body and completion of cytokinesis (Matuliene & Kuriyama, 2002; Zhu et al, 2005). In HeLa cells depleted of MKLP1, not only MKLP1 signals but also Arf6 signals on the Flemming body and its remnants disappear (Figure 6E); the population of multinucleate cells is increased as compared with control siRNA-treated cells (Figure 6H). Both the Arf6 delocalization and multinucleate phenotype are significantly rescued by exogenous expression of MKLP1(WT) or MKLP1(H758A), which retains the Arf6 binding ability. By contrast, expression of the Arf6 binding–defective mutant MKLP1(Y754A) apparently does not restore localization of Arf6 to the Flemming body and marginally rescues the multinucleate phenotype (Figure 6F-H).

The transient association of Arf6 with the cleavage furrow prior to its attachment to the Flemming body (Figures 1E and 3C, and Movies S1-S3) suggests that Arf6 is activated in a spatially specific manner when it is near the cleavage furrow. In this context, it is noteworthy that PtdIns4*P* 5-kinase and its product, PtdIns(4,5)$P_2$, accumulate near the cleavage furrow during cytokinesis (Emoto et al, 2005; Field et al, 2005). Previously, we showed that Arf6 can directly activate PtdIns4*P* 5-kinase (Honda et al, 1999). Because several Arf guanine-nucleotide exchange factors, including EFA6 (exchange factor for Arf6), have PH domains that bind PtdIns(4,5)$P_2$ (Derrien et al, 2002; Klarlund et al, 2000), Arf6 can be locally activated by these exchange factors. Thus, it is possible that a small increase in activated Arf6 leads to an amplification in the signal through a localized increase in the phosphoinositide.

How does Arf6 regulate cytokinesis? Arf6 may mediate, by vesicular transport, local delivery of membranes and specific proteins such as the exocyst complex, which allows targeting of vesicles to the plasma membrane domains where ingression and abscission occur (Prekeris & Gould, 2008; Steigemann & Gerlich, 2009). Arf6's role in cytokinesis may be primarily a matter of fine-tuning, since Arf6-KO MEFs retain the capacity for division, although the population of multinucleate cells is elevated.

***Comparison of interfaces between GTP-bound Arf6 and effector proteins***

The overall structure of the Arf6–cMKLP1 complex, including the β-sheet extending throughout

the complex, is unique among Arf–effector complexes. However, comparison between the Arf6–cMKLP1 complex and two Arf6–effector complexes, Arf6–CTA1 and Arf6–JIP4-LZII, whose structures have already been solved (Isabet et al, 2009; O'Neal et al, 2005), reveals some intriguing similarities (Figure 7A). First, the overall structures of Arf6 in complex with these effectors, as well as the monomeric Arf6–GTPγS structure (PDB 2J5X), are quite similar to one another, with an RMSD of 0.42 Å over all the Cα atoms. Thus, MKLP1 binding, or binding of effectors in general, does not significantly affect the conformation of the activated GTPase. Second, the same interface of Arf6, involving the Sw1, Sw2 and interswitch regions, is employed not only in its complex with cMKLP1 but also in its complexes with CTA1 and JIP4-LZII (Figures 5A and 7A), with the surface areas varying from 1658 $Å^2$ (Arf6–JIP4-LZII) to 2241 $Å^2$ (Arf6–cMKLP1) (Table S1). The corresponding surface regions of Arf1 and Arl (Arf-like) GTPases are also engaged in formation of complexes with their effectors (Figure 7B) (Hanzal-Bayer et al, 2002; Kawasaki et al, 2005; Panic et al, 2003; Shiba et al, 2003; Zhang et al, 2009). The interfaces between Arf/Arl molecules and their effectors include invariant hydrophobic residues that constitute the hydrophobic pocket, as well as the triad patch involved in effector binding (Chavrier & Ménétrey, 2010; Kawasaki et al, 2005; Ménétrey et al, 2007). In the Arf6–cMKLP1, Arf6–CTA1 and Arf6–JIP4-LZII complexes, these hydrophobic residues of Arf6 are largely conserved (Figures 5D and S2B).

Despite the extensive conservation of Arf6 residues involved in its interaction with effector proteins, the effector structures are quite different from one another (Figures 5A and 7A). The CTA1 interface includes an activation loop between an α-helix and a β-sheet (Kawasaki et al, 2005; O'Neal et al, 2005), and JIP4–LZII forms an all-helical homodimer that constitutes the interface for Arf6 (Isabet et al, 2009). The cMKLP1 interface is mainly composed of five β strands (Figures 4B and 5A). The two hydrogen bonds between $Phe47^{Arf6}$ within β2 and $Val786^{cMKLP1}$ within β5 make major contributions to the β-strand interaction (Figure 5E, G). In contrast, $Phe47^{Arf6}$ forms a water-mediated hydrogen bond with $Gly118^{CTA1}$ and a hydrogen bond with $Lys423^{JIP4}$ in only one (chains A/C) of the two complexes in the crystal (Isabet et al, 2009; O'Neal et al, 2005).

We have shown that the interaction between $Tyr77^{Arf6}$ and $Tyr754^{cMKLP1}$ is more critical for the formation and function of the Arf6–cMKLP1 complex than that between $His76^{Arf6}$ and $His758^{cMKLP1}$ (Figure

6). Tyr77$^{Arf6}$ is assigned as one of the key residues in the invariant hydrophobic triad (Figure 5D) (Chavrier & Ménétrey, 2010; Kawasaki et al, 2005; Ménétrey et al, 2007) and participates in direct hydrogen bond formation in the Arf6–cMKLP1 complex (the distance between OH atom of Tyr77$^{Arf6}$ and OH atom of Tyr754$^{cMKLP1}$ is 2.8 Å) (Figure 7C, left), whereas it makes a water-mediated hydrogen bond with Pro92$^{CTA1}$ or Asp419$^{JIP4}$. His76$^{Arf6}$ that has been identified as a residue of the hydrophobic pocket (Chavrier & Ménétrey, 2010; Kawasaki et al, 2005; Ménétrey et al, 2007) contributes less significantly to the cMKLP1 interaction than does Tyr77$^{Arf6}$. However, His76$^{Arf6}$ is indeed important for interactions with other effectors; it is one of the residues that form an effector-binding patch in the Arf6–CTA1 complex (O'Neal et al, 2005), and its carbonyl main chain forms an additional hydrogen bond to Lys417$^{JIP4}$ to further stabilize the Arf6–JIP4-LZII complex (Isabet et al, 2009). His76$^{Arf6}$ (His80$^{Arf1}$) is critical for the Arf interaction with the GGA1-GAT domain (Figure 7C, right). Superimposing the Arf6 structure on the Arf1–GGA1 complex (PDB 1J2J) (Shiba et al, 2003) reveals that His76$^{Arf6}$ forms a water-mediated hydrogen bond with Ser175$^{GGA1}$, whereas Tyr77$^{Arf6}$ can interact with GGA1 only through van der Waals contacts (Figure 7C, right). Thus, when His76$^{Arf6}$ is mutated, the van der Waals contacts of Tyr77$^{Arf6}$ are not sufficient to maintain the Arf6–GGA1 complex. By contrast, in the Arf6–cMKLP1 complex, His76$^{Arf6}$ forms a hydrogen bond with His758$^{cMKLP1}$, whereas Tyr77$^{Arf6}$ interacts with cMKLP1 through a hydrogen bond with Tyr754$^{cMKLP1}$ and through van der Waals contacts. It is therefore likely that the Tyr77$^{Arf6}$–Tyr754$^{cMKLP1}$ interaction is able to maintain the Arf6–cMKLP1 complex in the absence of the His76$^{Arf6}$–His785$^{cMKLP1}$ interaction (Figure 6A, B).

We then compared the Arf6–cMKLP1 structure with that of the Arl2–PDEδ complex (Hanzal-Bayer et al, 2002). Although β-sheet interactions contribute to formation of both complexes, a parallel β-sheet is formed in the Arl2–PDEδ complex (β2$^{Arl2}$–β7$^{PDEδ}$) (Figure 7B), while an antiparallel one in Arf6–cMKLP1 (β2$^{Arf6}$–β5$^{cMKLP1}$) (Figure 5). Furthermore, the residue that corresponds to His76$^{Arf6}$ is conserved in all Arfs, but not in Arl proteins, including Arl2 (Figure S1B). In the crystal structures, Asn79$^{Arl2}$ (corresponding to the His76$^{Arf6}$ position) has hydrophobic interactions with Phe96$^{PDEδ}$ and Ile98$^{PDEδ}$, and Tyr80$^{Arl2}$ (corresponding to Tyr77$^{Arf6}$) makes a hydrogen bond with the main-chain of Phe96$^{PDEδ}$. Overall, the molecular basis for the complex formation of Arf6–cMKLP1 is different from that of Arl2–PDEδ.

***Model for function of the Arf6–MKLP1 complex***

We propose that two molecules of activated Arf6 bind to each homodimer of MKLP1 at the Flemming body, resulting in a higher fidelity of cytokinesis. In the crystal, the Arf6–MKLP1 complex consists of a heterotetramer with two Arf6 and two MKLP1 molecules (Figure 4A). Our SAXS (Figure 4C) and cross-linking data (Figure S2) support the conclusion that the heterotetramer is present in solution and is not a crystallographic artifact. We speculate that the heterotetrameric Arf6–MKLP1 complex is anchored to membranes, most likely the plasma membrane, through myristoylated N-terminal helices of the two Arf6 molecules (Figure 8A). Note that each of the Arf6 molecules in the heterotetramer are positioned such that their N-terminal helices and covalently attached myristates, each of which are involved in membrane binding, are optimally positioned, pointed away from the rest of the MKLP1 molecule and toward a membrane anchoring site for the activated GTPase. This model suggests that on the Flemming body, Arf6 and the C-terminal domain of MKLP1 are positioned close to the membrane, while the N-terminal motor domain associates with the microtubule bundle (Figure 8A). The simultaneous association of the Arf6–MKLP1 complex with the microtubule bundle and the plasma membrane is indirectly supported by the observation that, after abscission, the Flemming body remnant migrates up along (probably beneath) the cortical membrane of a daughter cell (Figure 1E, red arrows, and Movie S1). The electrostatic surface potential map indicates that Arf6 binding to cMKLP1 enlarges its positively charged surface area relative to cMKLP1 alone (Figure 8B, top panels), making more favorable the association between the positively charged protein surface and negatively charged membrane surface. In this context, it is noteworthy that, as described above, PtdIns(4,5)$P_2$ accumulates around the cleavage furrow during cytokinesis (Emoto et al, 2005; Field et al, 2005). It will be therefore important to address whether membrane association of the Arf6–MKLP1 complex is under the regulation of changes in the local lipid composition.

There is another possible function of Arf6 at the Flemming body, although not mutually exclusive with the above model. We previously showed that Arf6-depleted cells accumulate FIP3-positive vesicles around the central spindle in early cytokinesis phase, but then failed to proceed with cytokinesis (Takahashi et al, 2011). On the other hand, Montagnac *et al.* (2009) have proposed that FIP3-positive endosomal vesicles are trafficked towards the plus ends of the central spindle in a kinesin-1/JIP4-dependent manner.

Together with the results in the present study, it is therefore possible that, through interacting with FIP3/4 or JIP3/4, Arf6 at the Flemming body serves as an acceptor for incoming endosomal vesicles, the accumulation of which is required for subsequent abscission (Prekeris & Gould, 2008; Schiel et al, 2011; Steigemann & Gerlich, 2009). We previously showed that, after abscission, FIP3 as well as Arf6 is incorporated into one of the daughter cells as a Flemming body remnant (Takahashi et al, 2011), supporting an interaction of FIP3 with Arf6 on the Flemming body. However, because an Arf6 molecule is unlikely to bind simultaneously to MKLP1 and FIP3/4 or JIP3/4, this model requires local switching of the Arf6 partners.

## MATERIALS AND METHODS

### *Cell culture, DNA transfection, and RNA interference*

MEFs were established from wild-type and Arf6-KO mice (Suzuki et al, 2006). Knockdown of MKLP1 was performed in a previously described manner (Ishizaki et al, 2008; Man et al, 2011). Briefly, a 3'-untranslated region of human MKLP1 cDNA was amplified using a primer set (5'-GCCATGAACTGACAGTCCCAG-3' and 5'-AGTGCTTTTGATTTTAATTCTTTTGG-3') and used for preparation of a pool of siRNAs with BLOCK-iT RNAi TOPO Transcription and Dicer RNAi kits (Invitrogen). HeLa cells grown on coverslips in a 3.5-cm dish were transfected with siRNAs (0.25 μg/dish) using Lipofectamine 2000 (Invitrogen) and incubated for 4 hr. The medium was then changed, and 48 hr after transfection the cells were processed for immunofluorescence and immunoblot analyses. For recovery experiments, a pCAG vector for HA-MKLP1 (0.4 μg/dish) was transfected into cells along with the siRNAs.

### *Pulldown assay*

*Escherichia coli* BL21(DE3) cells transformed with the GST fusion protein vector were treated with 0.1 mM IPTG for 4 hr at 25°C to induce protein expression, lysed and used to purify the recombinant protein with glutathione–Sepharose 4B beads (GE Healthcare). Lysates of HeLa cells expressing HA-tagged Arf were prepared as described previously (Man et al, 2011; Shiba et al, 2006; Takatsu et al, 2002) and incubated at 4°C for 2 hr with the GST-fusion protein coupled to glutathione–Sepharose 4B beads. The beads were washed four times with Hepes-based buffer, and subjected to SDS–PAGE and immunoblotting.

***Immunofluorescence microscopy and time-lapse imaging***

For immunofluorescence microscopy, cells were fixed, permeabilized and immunostained as described previously (Ishizaki et al, 2008; Shin et al, 2004; Takahashi et al, 2011). For time-lapse imaging, cells were placed on a microscope stage that had been pre-warmed at 37°C in a 5% $CO_2$ atmosphere. The cells were observed using EM-CCDs (Hamamatsu Photonics) on an Axiovert 200M microscope (Carl Zeiss). Images were acquired sequentially every 5 min and analyzed using IP-Lab™ ver. 4.0.8 (SOLUTION Systems). Three-dimensional time-lapse imaging was performed using an A1RMP confocal microscope (Nikon).

***Crystallization and data collection***

Crystallization conditions were initially searched using a crystallization robot (Hiraki et al, 2006). The final crystallization conditions for the native and Se-Met cMKLP1–Arf6 complexes were 12% w/v PEG 4000, 0.1 M sodium cacodylate, pH 6.5, 50 mM $(NH_4)_2SO_4$, 5 mM $MgCl_2$, 0.25-1.0% v/v ethyl acetate at 20°C. Crystals were then transferred to cryosolutions containing 20% glycerol or ethylene glycol. Data were collected at 100 K using beamline BL-5A or AR-NW12A at the Photon Factory, KEK (Tsukuba, Japan). All diffraction data were processed using HKL2000 (Otwinowski & Minor, 1997). Data collection and processing statistics are summarized in Table S2.

***Phasing, model building and refinement***

The MR-SAD method was applied to solving the Se-Met data of the Arf6–cMKLP1 complex (Schuermann & Tanner, 2003). An Arf6 structure (PDB 2J5X) was used as a molecular replacement (MR) template. The MR analysis was performed using Phaser (CCP4, 1994). The initial model was built using Buccaneer (CCP4, 1994) after density modification by DM or Parrot (CCP4, 1994). MR was applied to the native data using the Arf6–cMKLP1 complex structure generated from the Se-Met data, using Phaser. NCS restraints were applied during refinement before the final refinement. The final model was built with Coot (Emsley et al, 2010) and refined using Phenix (Adams et al, 2010) and REFMAC5 (CCP4, 1994) with TLS (Painter & Merritt, 2006) (Figure S5) at 3.0 Å resolution. There are four Arf6 (chains A, C, E, and G)–cMKLP1 (chains B, D, F, and H) complexes in the asymmetric unit. Finally, the refined structure of the Arf6–cMKLP1 complex was validated by MolProbity (Chen et al, 2010). The refinement statistics are

summarized in Table S1. Figures were drawn using MOLSCRIPT (Kraulis, 1991), Raster3D (Merritt & Bacon, 1997) , Pymol (Schrodinger, 2010) and CCP4MG (Potterton et al, 2004).

***SAXS experiments***

SAXS data were collected at BL-10C at the Photon Factory, KEK using bovine serum albumin (BSA) as a calibration standard. Arf6–cMKLP1 and BSA were dissolved in Buffer A. Protein concentrations varied within a range of 2.0–21.3 mg/ml. The sample cell was 50 μl in volume and had a 1 mm path-length. The X-ray wavelength was 1.488 Å, and the scattered X-rays were recorded by PSPC with an exposure of 600 sec at 900 mm from the sample position. Guinier analysis was carried out by the standard procedure (Guinier & Fournet, 1955). Data processing was performed using the IGOR Pro data analysis program (Wavemetrics). X-ray scattering intensities in the small-angle region are given as $I$ (Q) = $I$(0) exp ($-R_g^2Q^2/3$), where Q and $I$(0) are momentum transfer and the intensity at zero scattering angle, respectively. Q is defined by $Q = 4\pi\sin\theta/\lambda$, where $2\theta$ and $\lambda$ are the scattering angle and the wavelength of the X-rays, respectively. The radius of gyration ($R_g$) was obtained from the slope of the Guinier plot, which is a plot of ln[$I$(Q)] against $Q^2$.

***Accession Code***

Protein Data Bank: Coordinates for the Arf6–MKLP1 complex have been deposited with accession code 3VHX.

***Acknowledgments***

We thank Roger Tsien for providing materials, Richard Kahn for comments on the manuscript, Tamie Aoki and Tamami Uejima for technical support, and KEK-PF beamline staff for diffraction data collection. This work was supported in part by grants from the Ministry of Education, Culture, Sports, Science and Technology of Japan; the Japan Society for Promotion of Science; the Special Coordination Fund for Promoting Science and Technology; and the Targeted Proteins Research Program.

***Author Contributions***

H.M., T.T., M.O., S.T., H.T., Yo.K, A.H., T.U., Y.X. and H.K. participated in experimental work and data analysis. H.M., Ya.K., H.K., Mi.,K., H.-W.S., Ma.K., R.K., S.W. and K.N. participated in project planning. H.M., Y.K., H.-W.S., Ma.K., R.K., S.W. and K.N. wrote the manuscript.

***Conflict of Interest***

The authors declare that they have no conflict of interest.

**REFERENCES**

Adams PD, Afonine PV, Bunkoczi G, Chen VB, Davis IW, Echols N, Headd JJ, Hung LW, Kapral GJ, Grosse-Kunstleve RW, McCoy AJ, Moriarty NW, Oeffner R, Read RJ, Richardson DC, Richardson JS, Terwilliger TC, Zwart PH (2010) PHENIX: a comprehensive Python-based system for macromolecular structure solution. *Acta Crystallogr D* **66:** 213-221

Balasubramanian MK, Bi E, Glotzer M (2004) Comparative analysis of cytokinesis in budding yeast, fission yeast and animal cells. *Curr Biol* **14:** R806-R818

Boman AL, Kuai J, Zhu X, Chen J, Kuriyama R, Kahn RA (1999) Arf proteins binds to mitotic kinesin-like protein 1 (MKLP1) in a GTP-dependent fashion. *Cell Motil Cytoskeleton* **44:** 119-132

CCP4 (1994) The CCP4 suite: programs for protein crystallography. *Acta Crystallogr D* **50:** 760-763

Chavrier P, Ménétrey J (2010) Toward a structural understanding of Arf family: effector specificity. *Structure* **18:** 1552-1558

Chen VB, Arendall WB, III, Headd JJ, Keedy DA, Immormino RM, Kapral GJ, Murray LW, Richardson JS, Richardson DC (2010) MolProbity: all-atom structure validation for macromolecular crystallography. *Acta Crystallogr D* **66:** 12-21

D'Souza-Schorey C, Chavrier P (2006) ARF proteins: roles in membrane traffic and beyond. *Nat Rev Mol Cell Biol* **7:** 347-358

Derrien V, Couillault C, Franco M, Martineau S, Montcourrier P, Houlgatte R, Chavrier P (2002) A conserved C-terminal domain of EFA6-family ARF6-guanine nucleotide exchange factors induces lengthening of microvilli-like membrane protrusions. *J Cell Sci* **115:** 2867-2879

Dyer N, Rebollo E, Dominguez P, Elkhatib N, Chavrier P, Daviet L, González C, González-Gaitán M (2007) Spermatocyte cytokinesis requires rapid membrane addition mediated by ARF6 on central spindle recycling endosomes. *Development* **134:** 4437-4447

Emoto K, Inadome H, Kanaho Y, Narumiya S, Umeda M (2005) Local change in phospholipid composition at the cleavage furrow is essential for completion of cytokinesis. *J Biol Chem* **280:** 37901-37907

Emsley P, Lohkamp B, Scott WG, Cowtan K (2010) Features and development of Coot. *Acta Crystallogr D* **66:** 486-501

Field SJ, Madson N, Kerr ML, Galbraith KAA, Kennedy CE, Tahiliani M, Wilkins A, Cantley LC (2005) PtdIns(4,5)P2 functions at the cleavage furrow during cytokinesis. *Curr Biol* **15:** 1407-1412

Fielding AB, Schonteich E, Matheson J, Wilson G, Yu X, Hickson GRX, Srivastava S, Baldwin SA, Prekeris R, Gould GW (2005) Rab11-FIP3 and FIP4 interact with Arf6 and the exocyst to control membrane traffic in cytokinesis. *EMBO J* **24:** 3389-3399

Glotzer M (2005) The molecular requirements for cytokinesis. *Science* **307:** 1735-1739

Guinier A, Fournet G (1955) *Small-angle scattering of X-rays*, New York,: Wiley.

Hanzal-Bayer M, Renault L, Roversi P, Wittinghofer A, Hillig RC (2002) The complex of Arl2-GTP and PDE delta: from structure to function. *EMBO J* **21:** 2095-2106

Hiraki M, Kato R, Nagai M, Satoh T, Hirano S, Ihara K, Kudo N, Nagae M, Kobayashi M, Inoue M, Uejima T, Oda S, Chavas LM, Akutsu M, Yamada Y, Kawasaki M, Matsugaki N, Igarashi N, Suzuki M,

Wakatsuki S (2006) Development of an automated large-scale protein-crystallization and monitoring system for high-throughput protein-structure analyses. *Acta Crystallogr D* **62:** 1058-1065

Holm L, Rosenström P (2010) Dali server: conservation mapping in 3D. *Nucleic Acids Res* **38**(Web Server issue)**:** W545-549

Honda A, Nogami M, Yokozeki T, Yamazaki M, Nakamura H, Watanabe H, Kawamoto K, Nakayama K, Morris AJ, Frohman MA, Kanaho Y (1999) Phosphatidylinositol 4-phosphate 5-kinase $\alpha$ is a downstream effector of the small G protein ARF6 in membrane ruffle formation. *Cell* **99:** 521-532

Isabet T, Montagnac G, Regazzoni K, Raynal B, El Khadali F, England P, Franco M, Chavrier P, Houdusse A, Ménétrey J (2009) The structural basis of Arf effector specificity: the crystal structure of ARF6 in a complex with JIP4. *EMBO J* **28:** 2835-2845

Ishizaki R, Shin H-W, Mitsuhashi H, Nakayama K (2008) Redundant roles of BIG2 and BIG1, guanine-nucleotide exchange factors for ADP-ribosylation factors in membrane traffic between the trans-Golgi network and endosomes. *Mol Biol Cell* **19:** 2650-2660

Kahn RA, Cherfils J, Elias M, Lovering RC, Munro S, Schurmann A (2006) Nomenclature for the human Arf family of GTP-binding proteins: ARF, ARL, and SAR proteins. *J Cell Biol* **172:** 645-650

Kawasaki M, Nakayama K, Wakatsuki S (2005) Membrane recruitment of effector proteins by Arf and Rab GTPases. *Curr Opin Struct Biol* **15:** 681-689

Klarlund JK, Tsiaras W, Holik JJ, Chawla A, Czech MP (2000) Distinct phosphoinositide binding selectivities for pleckstrin homology domains of GRP1-like proteins based on diglycine *versus* triglycine motifs. *J Biol Chem* **275:** 32816-32821

Kraulis P (1991) MOLSCRIPT: a program to produce both detailed and schematic plots of protein structures. *J Appl Crystallogr* **24:** 946-950

Macia E, Luton F, Partisani M, Cherfils J, Chardin P, Franco M (2004) The GDP-bound form of Arf6 is located at the plasma membrane. *J Cell Sci* **117:** 2389-2398

Man Z, Kondo Y, Koga H, Umino H, Nakayama K, Shin H-W (2011) Arfaptins are localized to the *trans*-Golgi by interaction with Arl1, but not Arfs. *J Biol Chem* **286:** 11569-11578

Matuliene J, Kuriyama R (2002) Kinesin-like protein CHO1 is required for the formation of midbody matrix and the completion of cytokinesis in mammalian cells. *Mol Biol Cell* **13:** 1832-1845

Ménétrey J, Macia E, Pasqualato S, Franco M, Cherfils J (2000) Structure of Arf6-GDP suggests a basis for guanine nucleotide exchange factors specificity. *Nat Struct Biol* **7:** 466-469

Ménétrey J, Perderiset M, Cicolari J, Dubois T, Elkhatib N, El Khadali F, Franco M, Chavrier P, Houdusse A (2007) Structural basis for ARF1-mediated recruitment of ARHGAP21 to Golgi membranes. *EMBO J* **26:** 1953-1962

Merithew E, Hatherly S, Dumas JJ, Lawe DC, Heller-Harrison R, Lambright DG (2001) Structural plasticity of an invariant hydrophobic triad in the switch regions of Rab GTPases is a determinant of effector recognition. *J Biol Chem* **276:** 13982-13988

Merritt EA, Bacon DJ (1997) Raster3D: photorealistic molecular graphics. *Methods Enzymol* **277:** 505-524

Mishima M, Kaitna S, Glotzer M (2002) Central spindle assembly and cytokinesis require a kinesin-like

protein/RhoGAP complex with microtubule bundling activity. *Dev Cell* **2:** 41-54

Montagnac G, Sibarita J-B, Loubéry S, Daviet L, Romao M, Raposo G, Chavrier P (2009) ARF6 interacts with JIP4 to control a motor switch mechanism regulating endosome traffic in cytokinesis. *Curr Biol* **19:** 184-195

Neto H, Collins LL, Gould GW (2011) Vesicle trafficking and membrane remodelling in cytokinesis. *Biochem J* **437:** 13-24

O'Neal CJ, Jobling MG, Holmes RK, Hol WG (2005) Structural basis for the activation of cholera toxin by human ARF6-GTP. *Science* **309:** 1093-1096

Otwinowski Z, Minor W (1997) Processing of X-ray Diffraction Data Collected in Oscillation Mode. *Methods Enzymol* **276:** 307-326

Painter J, Merritt EA (2006) Optimal description of a protein structure in terms of multiple groups undergoing TLS motion. *Acta Crystallogr D* **62:** 439-450

Panic B, Perisic O, Veprintsev DB, Williams RL, Munro S (2003) Structural basis for Arl1-dependent targeting of homodimeric GRIP domains to the Golgi apparatus. *Mol Cell* **12:** 863-874

Pasqualato S, Menetrey J, Franco M, Cherfils J (2001) The structural GDP/GTP cycle of human Arf6. *EMBO Rep* **2:** 234-238

Pasqualato S, Renault L, Cherfils J (2002) Arf, Arl, Arp and Sar proteins: a family of GTP-binding proteins with a structural device for 'front-back' communication. *EMBO Rep* **3:** 1035-1041

Potterton L, McNicholas S, Krissinel E, Gruber J, Cowtan K, Emsley P, Murshudov GN, Cohen S, Perrakis A, Noble M (2004) Developments in the CCP4 molecular-graphics project. *Acta Crystallogr D* **60:** 2288-2294

Prekeris R, Gould GW (2008) Breaking up is hard to do: membrane traffic in cytokinesis. *J Cell Sci* **121:** 1569-1576

Schiel JA, Park K, Morphew MK, Reid E, Hoenger A, Prekeris R (2011) Endocytic membrane fusion and buckling-induced microtubule severing mediate cell abscission. *J Cell Sci* **124:** 1411-1424

Schonteich E, Pilli M, Simon GC, Matern HT, Junutula JR, Sentz D, Holmes RK, Prekeris R (2007) Molecular characterization of Rab11-FIP3 binding to ARF GTPases. *Eur J Cell Biol* **86:** 417-431

Schrodinger, LLC. (2010) The PyMOL Molecular Graphics System, Version 1.3r1.

Schuermann JP, Tanner JJ (2003) MRSAD: using anomalous dispersion from S atoms collected at Cu Kalpha wavelength in molecular-replacement structure determination. *Acta Crystallogr D* **59:** 1731-1736

Schweitzer JK, D'Souza-Schorey C (2002) Localization and activation of the ARF6 GTPase during cleavage furrow ingression and cytokinesis. *J Biol Chem* **277:** 27210-27216

Schweitzer JK, D'Souza-Schorey C (2005) A requirement for ARF6 during the completion of cytokinesis. *Exp Cell Res* **311:** 74-83

Shiba T, Kawasaki M, Takatsu H, Nogi T, Matsugaki N, Igarashi N, Suzuki M, Kato R, Nakayama K, Wakatsuki S (2003) Molecular mechanism of membrane recruitment of GGA by ARF in lysosomal protein transport. *Nat Struct Biol* **10:** 386-393

Shiba T, Koga H, Shin H-W, Kawasaki M, Kato R, Nakayama K, Wakatsuki S (2006) Structural basis for Rab11-dependent membrane recruitment of family of Rab11-interacting protein (FIP3)/Arfophilin-1. *Proc Natl Acad Sci USA* **103:** 15416-15421

Shin H-W, Morinaga N, Noda M, Nakayama K (2004) BIG2, a guanine nucleotide exchange factor for ADP-ribosylation factors: its localization to recycling endosomes and implication in the endosome integrity. *Mol Biol Cell* **15:** 5283-5294

Steigemann P, Gerlich DW (2009) Cytokinetic abscission: cellular dynamics at the midbody. *Trends Cell Biol* **19:** 606-616

Suzuki T, Kanai Y, Hara T, Sasaki J, Sasaki T, Kohara M, Maehama T, Taya C, Shitara H, Yonekawa H, Frohman MA, Yokozeki T, Kanaho Y (2006) Crucial role of the small GTPase ARF6 in hepatic cord formation during liver development. *Mol Cell Biol* **26:** 6149-6156

Takahashi S, Takei T, Koga H, Takatsu H, Shin H-W, Nakayama K (2011) Distinct roles of Rab11 and Arf6 in the regulation of Rab11-FIP3/Arfophilin-1 localization in mitotic cells. *Genes Cells* **16:** 938-950

Takatsu H, Yoshino K, Toda K, Nakayama K (2002) GGA proteins associate with Golgi membranes through interaction between their GGAH domains and ADP-ribosylation factors. *Biochem J* **365:** 369-378

Yu X, Prekeris R, Gould GW (2007) Role of endosomal Rab GTPases in cytokinesis. *Eur J Cell Biol* **86:** 25-35

Zhang T, Li S, Zhang Y, Zhong C, Lai Z, Ding J (2009) Crystal structure of the ARL2-GTP-BART complex reveals a novel recognition and binding mode of small GTPase with effector. *Structure* **17:**

602-610

Zhu C, Bossy-Metzel E, Jiang W (2005) Recruitment of MKLP1 to the spindle midzone/midbody by INCENP is essential for midbody formation and completion of cytokinesis in human cells. *Biochem J* **389:** 373-381

## FIGURE LEGENDS

**Figure 1. Localization of Arf6 to the Flemming body and phenotype of Arf6-KO cells**

(A) HeLa cells transfected with an expression vector for C-terminally mCherry-tagged Arf1, Arf3, Arf5 or Arf6 were stained with anti-β-tubulin antibody. (B) The cells in late cytokinesis phase in the experiment shown in (A) were classified as those with and without Arf-mCherry signals at the Flemming body. Percentages of cells with Arf signals at the Flemming body are expressed as bar graphs. (C) HeLa cells transfected with an expression vector for C-terminally EGFP-tagged Arf6(WT), Arf6(Q67L) or Arf6(T27N) were immunostained for β-tubulin. (D) The cells in late cytokinesis phase in the experiment shown in (C) were classified as those with and without Arf6-EGFP signals at the Flemming body. Percentages of cells with Arf6-EGFP signals are expressed as bar graphs. (E) Images from a three-dimensional time-lapse series of HeLa cells expressing Arf6-EGFP. HeLa cells transfected with an expression vector for Arf6-EGFP were subjected to three-dimensional time-lapse recording. Representative images from Movie S1 are shown. Left and right images, rotated by 90° with respect to the z axis, show the same two cells (cells identified by yellow and magenta asterisks). Cyan, green and red arrows indicate Arf6-EGFP signals on the cleavage furrow, Flemming body and its remnant, respectively. (F) Multinucleate phenotype of Arf6-KO MEFs. Wild-type or Arf6-KO MEFs were stained with anti-β-tubulin to reveal microtubules (red) and SYTOX Green to reveal nuclei. (G) Increase in the population of multinucleate cells by Arf6 knockout. The cells in the experiment shown in (F) were classified as mono-, bi-, and multinucleate (≥3 nuclei), and counted. Percentages of bi- and multinucleate cells in four independent examinations are expressed as bar graphs. In (A), (C) and (F); bars, 10 μm.

**Figure 2. Interaction of MKLP1 with Arf6 *in vitro***

(A) Domain organization and comparison of the structures of the long and short forms of MKLP1. (B) A MKLP1 region encompassing residues 690–807 is responsible for interaction with Arf6. Lysates of HeLa cells expressing C-terminally HA-tagged Arf6(Q67L) were pulled down with GST, GST-MKLP1(690-807) (cMKLP1) or GST-MKLP1(690-789) and subjected to immunoblotting with anti-HA antibody. (C) GTP-bound Arf6 interacts with MKLP1. Lysates of HeLa cells expressing

C-terminally HA-tagged Arf6(WT), Arf6(Q67L), or Arf6(T27N) were pulled down with GST or GST-cMKLP1 and subjected to immunoblotting with anti-HA antibody. (D) MKLP1 interacts with all Arf isoforms examined. Lysates of HeLa cells expressing C-terminally HA-tagged Arf1(Q71L), Arf3(Q71L), Arf5(Q71L), or Arf6(Q67L) were pulled down with GST or GST-cMKLP1 and subjected to immunoblotting with anti-HA antibody. (E) SPR analysis of the GST-cMKLP1 interaction with Arf1, Arf3, Arf5 or Arf6. Steady-state resonance ($R_{eq}$) levels were plotted against each Arf concentration. $K_d$ values were calculated from the fitted curves.

**Figure 3. Colocalization of Arf6 and MKLP1 on the Flemming body and Arf6-independent localization of MKLP1**

(A) Localization of endogenous Arf6 and MKLP1 during cytokinesis. HeLa cells were processed for triple immunostaining for Arf6, MKLP1 and α-tubulin. Note that Arf6 was found on the Flemming body in cells in later phase of cytokinesis (lower row), but not in early phase (upper row), as judged by the width of the central spindle. (B) The cells in early and late cytokinesis phases in the examination shown in (A) were classified as those with and without Arf6 signals at the Flemming body. Percentages of cells with Arf6-EGFP signals are expressed as bar graphs. (C) A time-lapse analysis of HeLa cells expressing Arf6-EGFP and mRFP-MKLP1. An image sequence from Movie S3 is shown. HeLa cells transfected with expression vectors for Arf6-EGFP and mRFP-MKLP1 were subjected to time-lapse recording. (D) Normal Flemming body localization of MKLP1 in Arf6-KO cells. Wild-type or Arf6-KO MEFs were doubly immunostained for MKLP1 and β-tubulin. In (A) and (D); bars, 10 μm.

**Figure 4. Overall structure and SAXS experiments of the Arf6–cMKLP1 complex**

(A) Cartoon representation of the heterotetrameric Arf6–cMKLP1 complex is shown in two orthogonal views (side and bottom views). The two Arf6 molecules are colored in yellow and pink, and the two cMKLP1 molecules colored in orange and green. The βA region is colored in royal blue. In each Arf6 molecule, a GTP molecule and $Mg^{2+}$ are rendered using ball and stick representations. (B) Schematic representation of the heterotetrameric Arf6–cMKLP1 complex structure. Arf6 and cMKLP1 proteins are

colored in the same way as in (A). In Arf6, Sw1, interswitch and Sw2 regions were colored in purple, red, and cyan, respectively. One Arf6–cMKLP1 complex is indicated by a dashed line enclosure. The region shaded in grey shows the inter-protein β-sheet extending the entire Arf6–cMKLP1 complex. The βA-region colored in royal blue is represented as making a small β-sheet in the heterotetrameric Arf6–cMKLP1 complex structure. (C) Results of SAXS measurements of the Arf6–cMKLP1 complex. Guinier analysis shows that the values of $R_g$ and $I(0)$ increase as a function of the protein concentration. At the lowest concentration, the apparent molecular weight of the complex was estimated to be 26 kDa, slightly lower than the value (33 kDa) calculated from the amino acid sequence, still suggesting a 1:1 complex. At higher protein concentrations, the apparent molecular weight reaches a value approximately twice that of the heterodimer, indicating a 2:2 heterotetramer in solution. (left) Guinier plots of Arf6–cMKLP1 complex. (middle) Concentration dependence of $R_g^2$. $R_g^2$ for the Arf6–cMKLP1 complex was plotted against protein concentration. (right) Concentration dependence of $I(0)$/conc for the Arf6-cMKLP1 complex.

**Figure 5. Interaction between Arf6 and cMKLP1 in the complex**

(A) Overall structure of a heterodimeric portion of the Arf6–cMKLP1 complex. In this and following panels, cMKLP1 is shown in orange, and Arf6 is shown in yellow with Sw1 (purple), interswitch (red) and Sw2 (cyan). A GTP molecule and $Mg^{2+}$ are represented by ball-and-stick models. (B) Structure of GTP-bound Arf6 alone, or along with β4- and β5-strands of cMKLP1. The outer portion of the switch region of Arf6 is enclosed by a dashed square. (C) Structure of GDP-bound Arf6 alone or along with β4- and β5-strands of cMKLP1. GDP-Arf6 (PDB 1E0S) is superimposed on GTP-Arf6 in the Arf6–cMKLP1 complex. The conformational changes in the Sw1 region create an additional β-strand (β2') in the GDP-Arf6 structure. The β2'-strand of GDP-Arf6 overlaps with the β5-strand of cMKLP1, making it impossible for GDP-Arf6 to bind cMKLP1. (D) Schematic representation of the interface between Arf6 and cMKLP1. Boxes, arrows and lines represent helices, β-strands and loops, respectively. $Phe788^{cMKLP1}$, located between Sw1 and Sw2, is labeled in black letters in the hexagon, and two other important residues ($Tyr754^{cMKLP1}$ and $His758^{cMKLP1}$) on $\beta3^{cMKLP1}$ are labeled in black letters. Residues of the effector-binding patch on Arf6 are also labeled in black letters. The hydrophobic residues of the triad patch ($Phe47^{Arf6}$, $Trp62^{Arf6}$, and $Tyr77^{Arf6}$)

are labeled in black letters and underlined. (E) Interaction between $\beta2^{Arf6}$ and $\beta5^{cMKLP1}$. Secondary structure elements are drawn as cartoons and residues involved in the binding as sticks. Hydrogen bonds are represented as black dashed lines. (F) Interaction between $His76^{Arf6}$ and $His758^{cMKLP1}$. (G) Interaction between $Tyr77^{Arf6}$ and $Tyr754^{cMKLP1}$ in the hydrophobic triad patch region.

**Figure 6. Mutational analysis of the Arf6–MKLP1 interaction and Arf6 localization to the Flemming body**

(A) Tyr77 of Arf6 is important for Arf6's interaction with MKLP1. Lysates of HeLa cells expressing C-terminally HA-tagged Arf6(Q67L), Arf6(Q67L/Y77A) or Arf6(Q67L/H76A) were pulled down with GST, GST-cMKLP1, GST-GGA1(GAT), GST-FIP4(484-613) or GST-JIP4(LZII) and subjected to immunoblotting with anti-HA antibody. (B) Tyr754 of MKLP1 is important for MKLP1's interaction with Arf6. Lysates of HeLa cells expressing Arf6(Q67L)-HA were pulled down with GST, GST-GGA2(GAT), GST-FIP4(484-613), or wild type, Y754A mutant, or H758A mutant of GST-cMKLP1, and subjected to immunoblotting with anti-HA antibody. (C) HeLa cells transfected with an expression vector for Arf6(WT)-EGFP, Arf6(H76A)-EGFP or Arf6(Y77A)-EGFP were doubly stained with anti-MKLP1 and anti-β-tubulin. In this experiment, we used the Arf6(H76A) and Arf6(Y77A) mutants in the context of Q67L. (D) The cells in late cytokinesis phase in the experiment shown in (C) were classified as those with and without Arf6-EGFP signals at the Flemming body. Percentages of cells with Arf6-EGFP signals are expressed as bar graphs. (E) MKLP1-dependent localization of Arf6 to the Flemming body. HeLa cells treated with a pool of siRNAs for LacZ (siControl) or MKLP1 were triply immunostained for MKLP1 (green), Arf6 (red), and α-tubulin (blue). Note that a number of the control cells exhibit both the MKLP1 and Arf6 signals on the Flemming body or its remnant. (F) HeLa cells were transfected with an expression vector for HA-MKLP1(WT), HA-MKLP1(Y754A), or HA-MKLP1(H758A), together with siRNAs for MKLP1. After 48 hr, the cells were fixed and triply immunostained for HA, Arf6 and β-tubulin. (G) The cells in late cytokinesis phase in the experiment shown in (F) were classified as those with and without Arf6 signals at the Flemming body. Percentages of cells with Arf6-EGFP signals are expressed as bar graphs. (H) The control siRNA-treated cells and MKLP1 siRNA-treated cells with exogenous

expression of EGFP or an HA-MKLP1 construct in the experiment shown in (F) were classified as mono-, bi- and multinucleate (≥3 nuclei), and counted. Percentages of bi- and multinucleate cells are expressed as bar graphs. In (C), (E) and (F), bars, 10 μm.

**Figure 7. Structures of complexes of Arf and Arl proteins with their effectors**

(A) Interfaces of Arf6 for CTA1 and JIP4-LZII. The orientation of the Arf6 molecule is the same as that in the Arf6–cMKLP1 complex (Figure 5A), and coloring of Arf6 regions and representation of a GTP molecule and $Mg^{2+}$ are the same as in Figure 5A. CTA1 is colored in orange (left), and helices of the JIP4-LZII dimer are in orange and green (right). (B) Structures of Arf/Arl complexes with their effector proteins as indicated. The orientation of the Arf/Arl molecule is the same as in the Arf6–cMKLP1 complex (Figure 5A); coloring of Arf/Arl regions and representation of GTP and $Mg^{2+}$ are the same as in Figure 5A. The effector proteins are colored in orange. (C) The interfaces between Arf6/Arf1 and cMKLP1 (left) and between Arf1/Arf6 and the GGA1-GAT domain (right) are shown. Arf6, Arf1, cMKLP1 and GGA1 are colored in yellow, green, orange and magenta, respectively. In the left panel, the Arf1 molecule in the Arf1–GGA1 complex (PDB 1J2J) is superimposed on Arf6 of the Arf6–cMKLP1 complex, and black dashed lines indicate hydrogen bonds between Arf6 and cMKLP1. In the right panel, a red ball represents a water molecule (Wat212), black dashed lines indicate hydrogen bonds between GGA1 and Arf1 via Wat212, and a yellow dashed line indicates a hydrogen bond between Arf6 and Wat212.

**Figure 8. Model for membrane and microtubule interactions of the Arf6–MKLP1 complex and its electrostatic potential**

(A) Model for simultaneous interactions of the heterotetrameric Arf6–MKLP1 complex with membrane and microtubules. During cytokinesis, the complex is likely to be anchored to the plasma membrane, and the MKLP1 motor domain is associated with microtubules of the Flemming body. MKLP1 molecules are colored in green, orange and royal blue. Arf6 molecules are colored in yellow and pink with schematically represented N-terminal helices, and their myristates are represented as doted lines. The numbered arrows indicate viewing directions in (B). (B) The electrostatic potential representations of MKLP1 and the

Arf6–cMKLP1 complex, colored according to the calculated surface potential, from −10 kT (red) to 10 kT (blue).

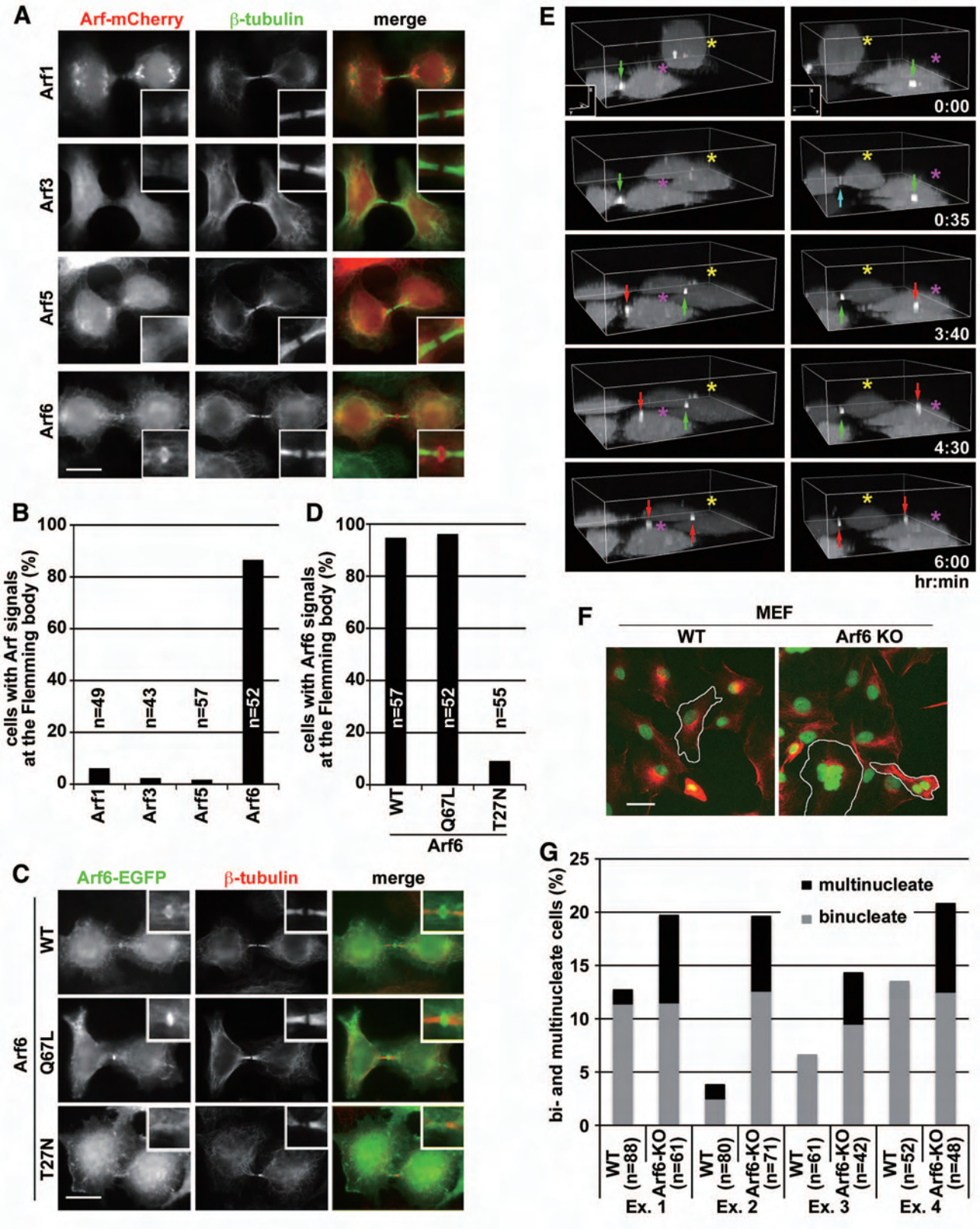
A
Arf-mCherry
β-tubulin
merge
Arf1
Arf3
Arf5
Arf6
B
cells with Arf signals at the Flemming body (%)
n=49
n=43
n=57
n=52
Arf1
Arf3
Arf5
Arf6
C
Arf6-EGFP
β-tubulin
merge
Arf6
WT
Q67L
T27N
D
cells with Arf6 signals at the Flemming body (%)
n=57
n=52
n=55
WT
Q67L
T27N
Arf6
E
0:00
0:35
3:40
4:30
6:00
hr:min
F
MEF
WT
Arf6 KO
G
bi- and multinucleate cells (%)
multinucleate
binucleate
WT (n=88)
Arf6-KO (n=61)
WT (n=80)
Arf6-KO (n=71)
WT (n=61)
Arf6-KO (n=42)
WT (n=52)
Arf6-KO (n=48)
Ex. 1
Ex. 2
Ex. 3
Ex. 4

**Figure 1**

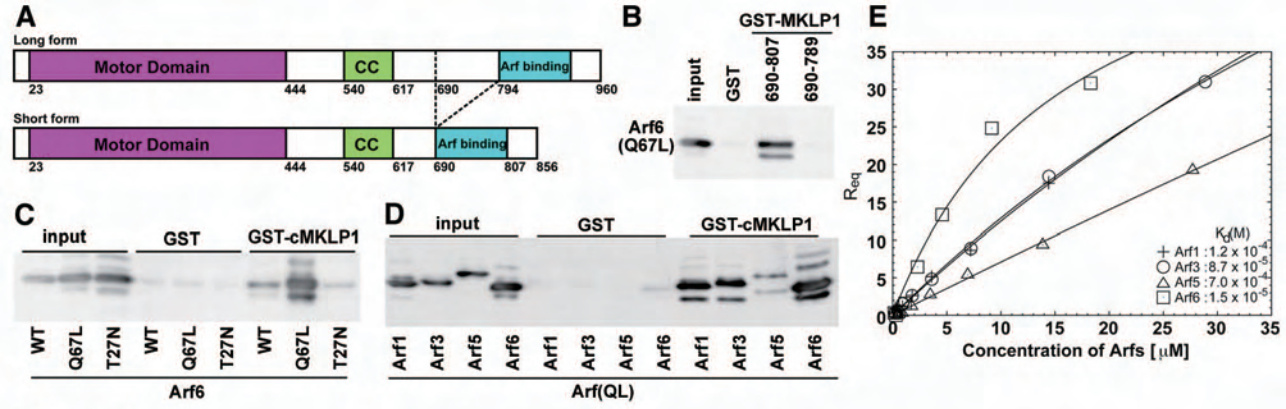
A
Long form
Motor Domain
CC
Arf binding
23
444
540
617
690
794
960
Short form
Motor Domain
CC
Arf binding
23
444
540
617
690
807
856
B
GST-MKLP1
input
GST
690-807
690-789
Arf6
(Q67L)
C
input
GST
GST-cMKLP1
WT
Q67L
T27N
WT
Q67L
T27N
WT
Q67L
T27N
Arf6
D
input
GST
GST-cMKLP1
Arf1
Arf3
Arf5
Arf6
Arf1
Arf3
Arf5
Arf6
Arf1
Arf3
Arf5
Arf6
Arf(QL)
E
Req
Kd(M)
Arf1 :1.2 x 10-4
Arf3 :8.7 x 10-5
Arf5 :7.0 x 10-4
Arf6 :1.5 x 10-5
Concentration of Arfs [μM]

**Figure 2**

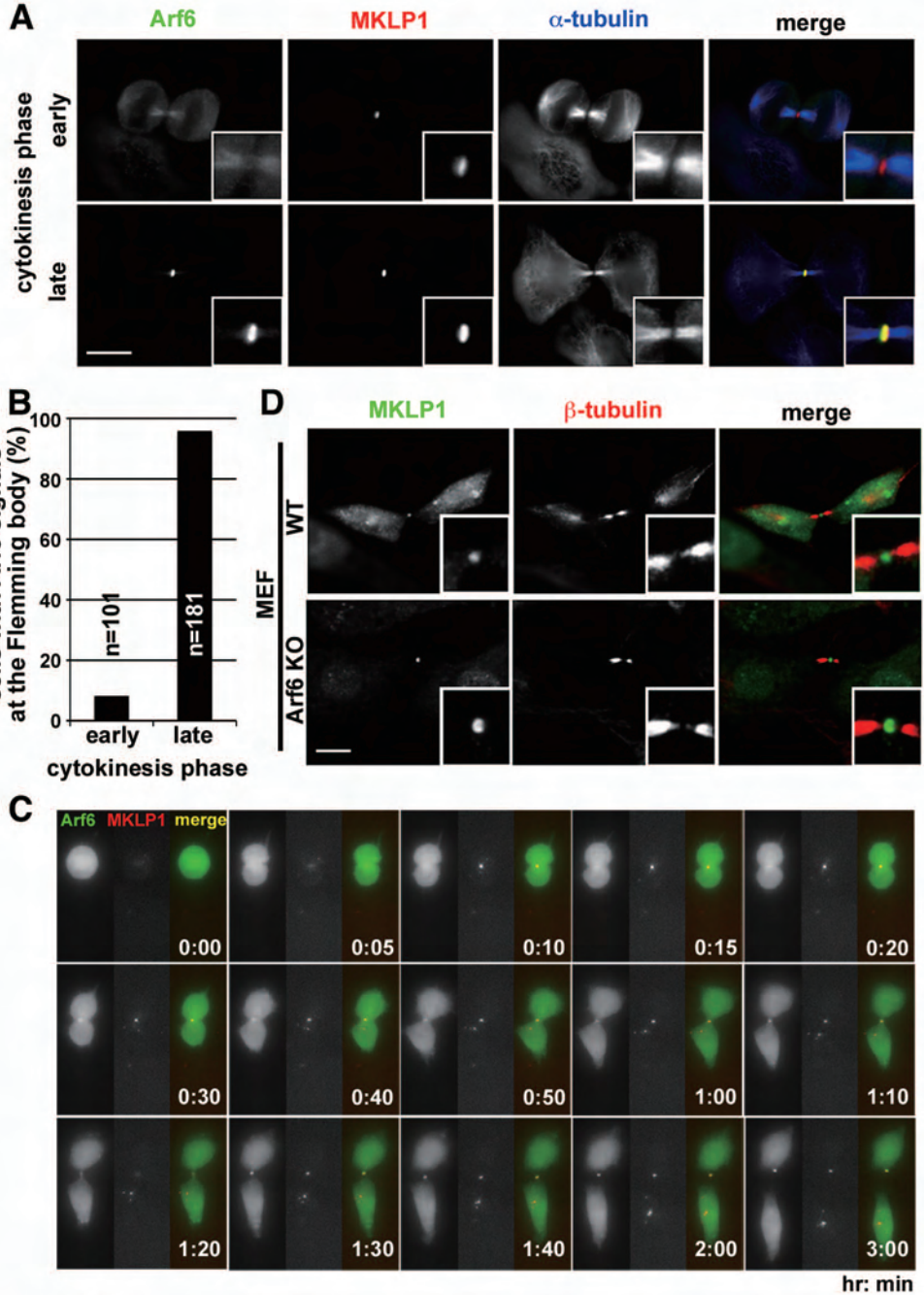
A
Arf6
MKLP1
α-tubulin
merge
cytokinesis phase
early
late
B
cells with Arf6 signals at the Flemming body (%)
100
80
60
40
20
0
n=101
n=181
early
late
cytokinesis phase
D
MKLP1
β-tubulin
merge
MEF
WT
Arf6 KO
C
Arf6 MKLP1 merge
0:00
0:05
0:10
0:15
0:20
0:30
0:40
0:50
1:00
1:10
1:20
1:30
1:40
2:00
3:00
hr: min

Figure 3

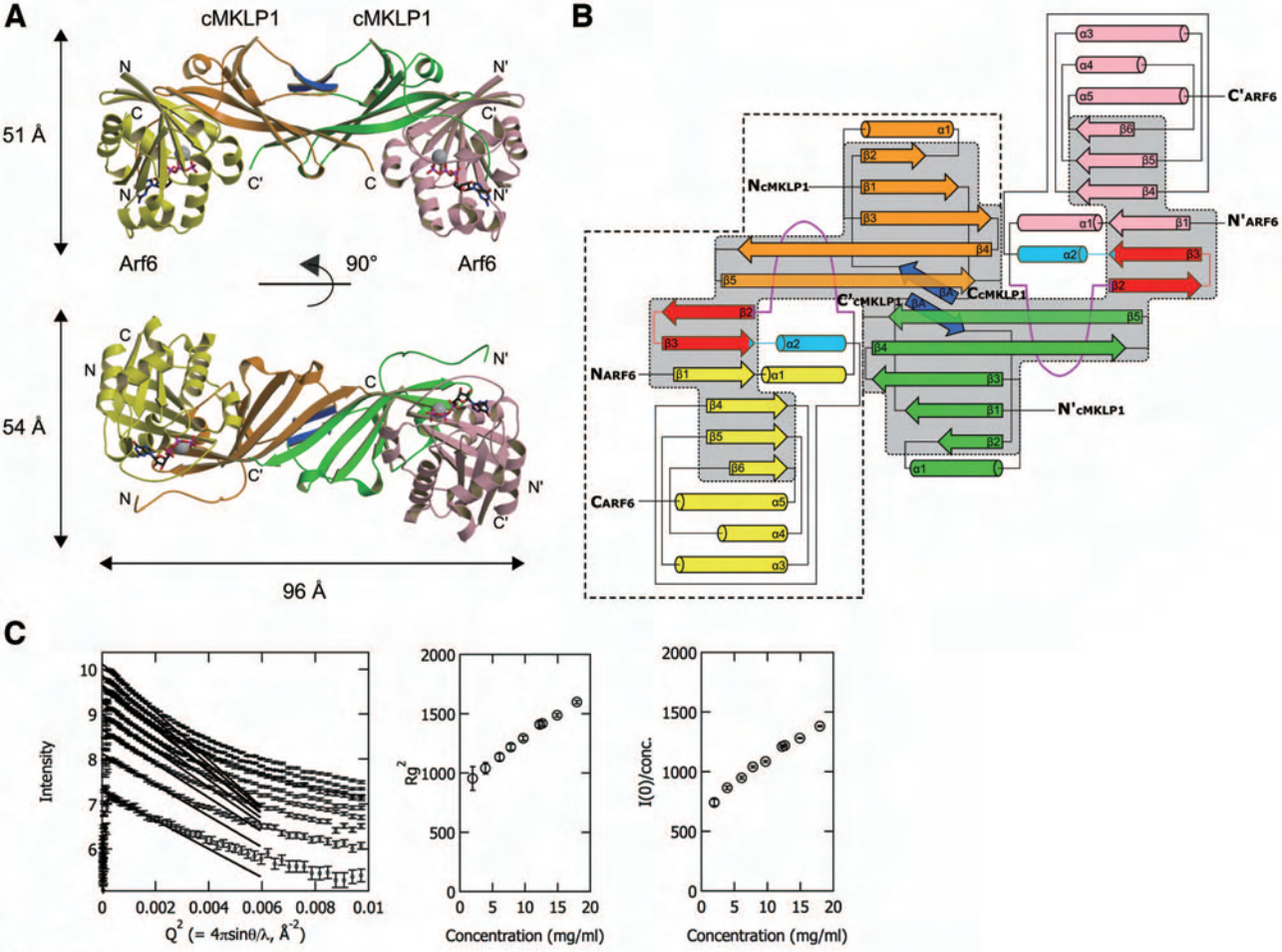
A
cMKLP1
cMKLP1
N
N'
C
C'
C'
C
N
N'
51 Å
Arf6
90°
Arf6
C
N
N'
C
C'
N
N'
C'
54 Å
96 Å
B
α3
α4
α5
C'ARF6
β6
β5
β4
α1
β1
N'ARF6
α2
β3
β2
NcMKLP1
α1
β2
β1
β3
β4
β5
C'cMKLP1
β6
CcMKLP1
β2
β5
β3
α2
β4
NARF6
β1
α1
β3
N'cMKLP1
β1
β2
α1
β4
β5
β6
CARF6
α5
α4
α3
C
Intensity
10
9
8
7
6
0
0.002
0.004
0.006
0.008
0.01
Q2 (= 4πsinθ/λ, Å-2)
Rg2
2000
1500
1000
500
0
0
5
10
15
20
Concentration (mg/ml)
I(0)/conc.
2000
1500
1000
500
0
0
5
10
15
20
Concentration (mg/ml)

**Figure 4**

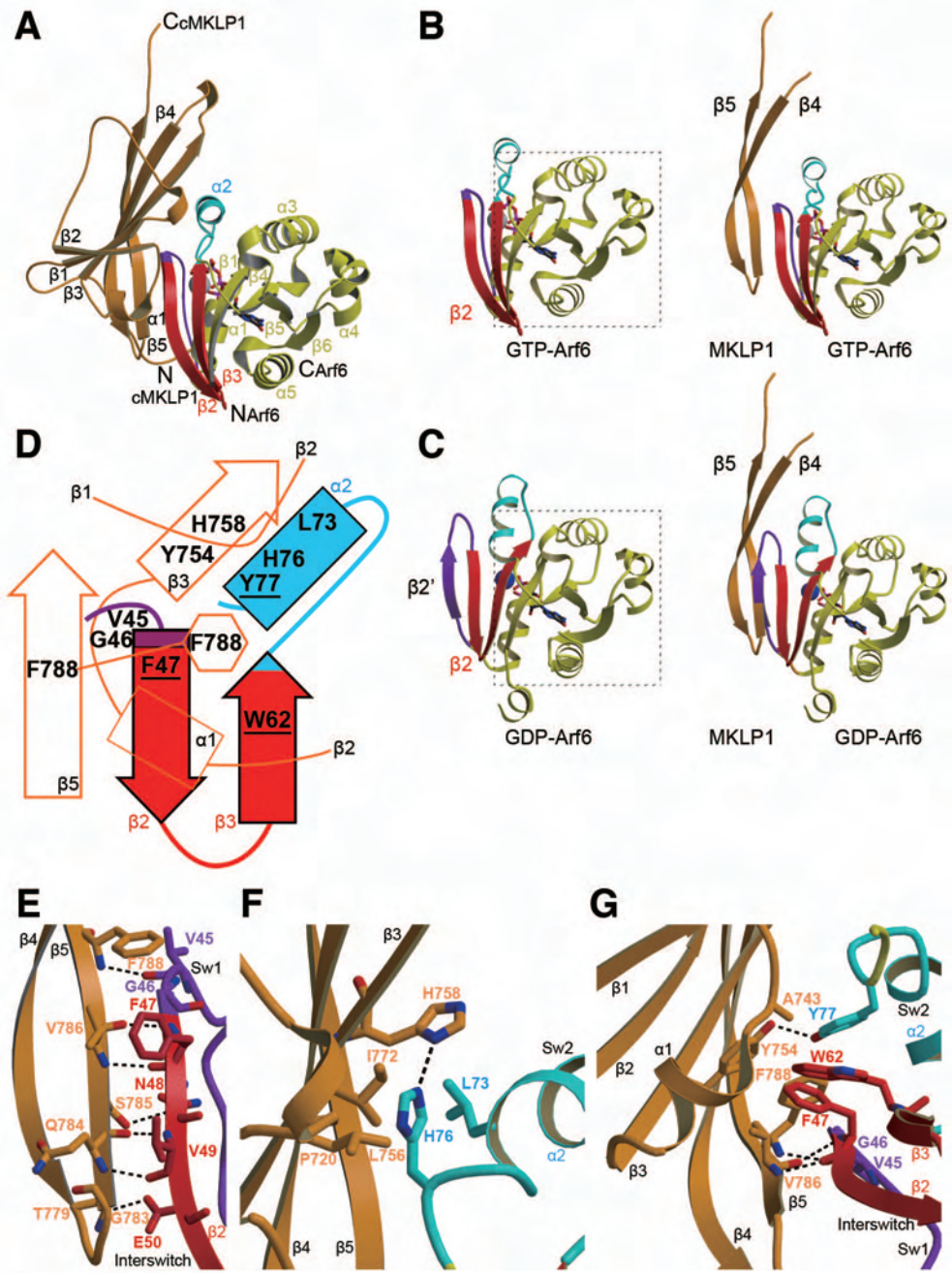
A
CcMKLP1
β4
α2
α3
β2
β1
β3
α1
β5
N
cMKLP1
β2
β1
β4
α1
β5
α4
β6
CArf6
β3
α5
NArf6
B
β2
GTP-Arf6
β5
β4
MKLP1
GTP-Arf6
D
β2
β1
α2
H758
L73
Y754
H76
β3
Y77
V45
G46
F788
F788
F47
W62
α1
β2
β5
β2
β3
C
β2'
β2
GDP-Arf6
β5
β4
MKLP1
GDP-Arf6
E
β4
β5
V45
F788
Sw1
G46
F47
V786
N48
S785
Q784
V49
T779
G783
β2
E50
Interswitch
F
β3
H758
I772
Sw2
L73
H76
α2
P720
L756
β4
β5
G
β1
A743
Y77
Sw2
α2
α1
Y754
W62
β2
F788
F47
G46
β3
V45
β3
V786
β2
β5
Interswitch
β4
Sw1

**Figure 5**

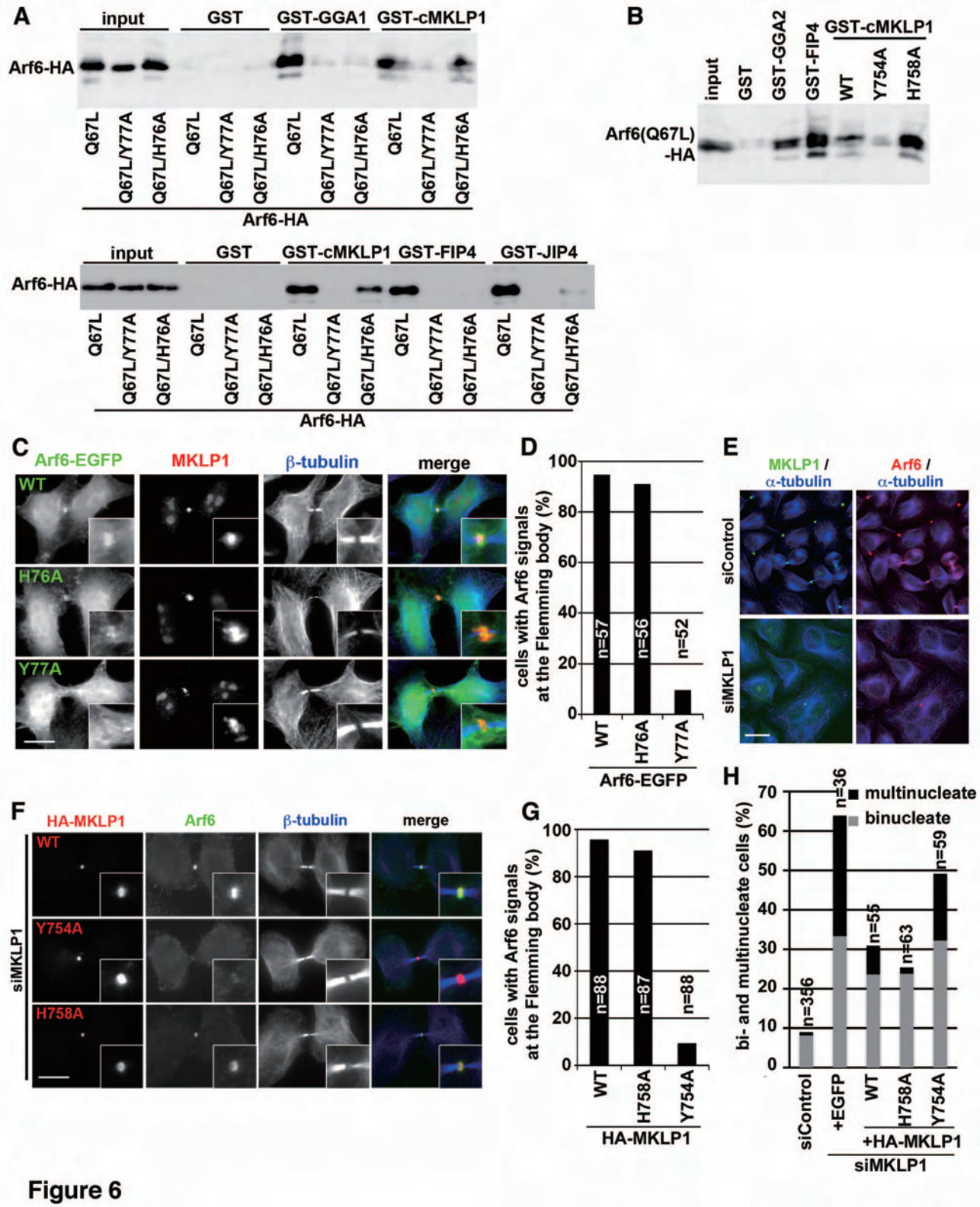
A
input
GST
GST-GGA1
GST-cMKLP1
Arf6-HA
Q67L
Q67L/Y77A
Q67L/H76A
Arf6-HA
input
GST
GST-cMKLP1
GST-FIP4
GST-JIP4
Arf6-HA
Arf6-HA
B
input
GST
GST-GGA2
GST-FIP4
GST-cMKLP1
WT
Y754A
H758A
Arf6(Q67L)
-HA
C
Arf6-EGFP
MKLP1
β-tubulin
merge
WT
H76A
Y77A
D
cells with Arf6 signals at the Flemming body (%)
n=57
n=56
n=52
WT
H76A
Y77A
Arf6-EGFP
E
MKLP1 / α-tubulin
Arf6 / α-tubulin
siControl
siMKLP1
F
HA-MKLP1
Arf6
β-tubulin
merge
siMKLP1
WT
Y754A
H758A
G
cells with Arf6 signals at the Flemming body (%)
n=88
n=87
n=88
WT
H758A
Y754A
HA-MKLP1
H
bi- and multinucleate cells (%)
multinucleate
binucleate
n=356
n=36
n=55
n=63
n=59
siControl
+EGFP
WT
H758A
Y754A
+HA-MKLP1
siMKLP1

**Figure 6**

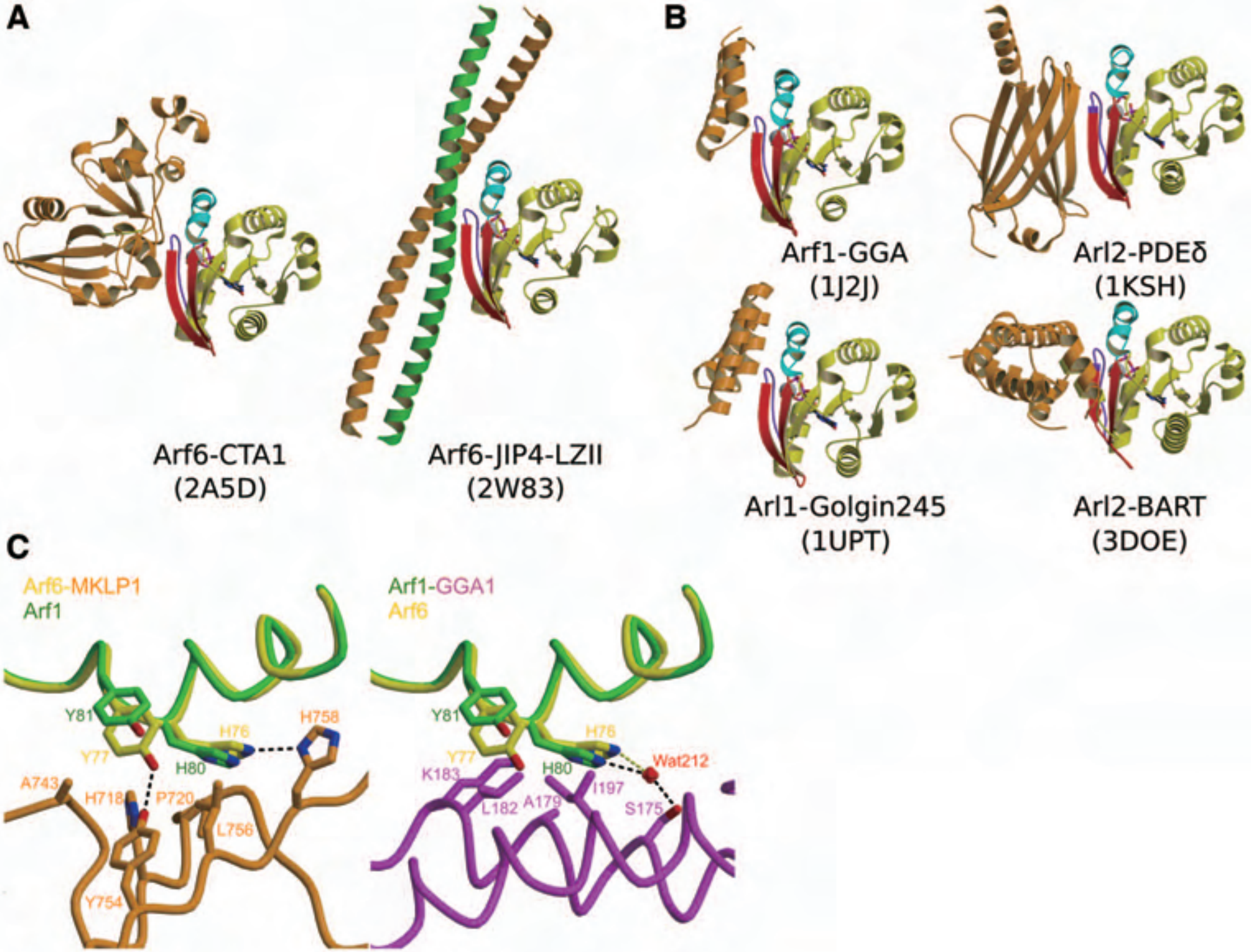
A
Arf6-CTA1
(2A5D)
Arf6-JIP4-LZII
(2W83)
B
Arf1-GGA
(1J2J)
Arl2-PDEδ
(1KSH)
Arl1-Golgin245
(1UPT)
Arl2-BART
(3DOE)
C
Arf6-MKLP1
Arf1
Y81
H76
H758
Y77
H80
A743
H718
P720
L756
Y754
Arf1-GGA1
Arf6
Y81
H76
Y77
Wat212
K183
H80
I197
L182
A179
S175

**Figure 7**

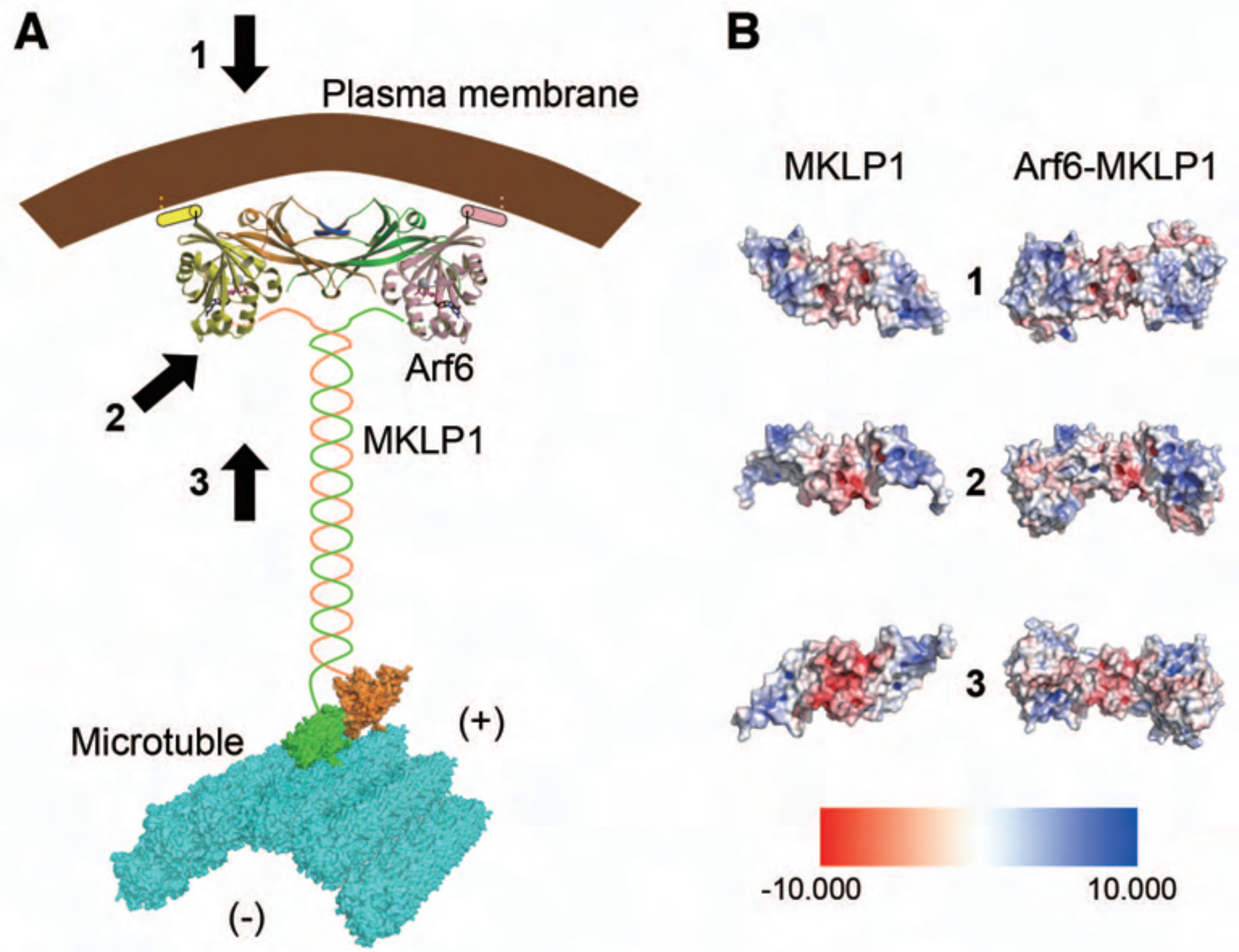
A
1
Plasma membrane
Arf6
2
MKLP1
3
Microtuble
(+)
(-)
B
MKLP1
Arf6-MKLP1
1
2
3
-10.000
10.000

**Figure 8**

**SUPPLEMENTARY INFORMATION**

# Structural basis for Arf6–MKLP1 complex formation on the Flemming body responsible for cytokinesis

**Hisayoshi Makyio[1,*], Minako Ohgi[2,*], Tomomi Takei[2,*], Senye Takahashi[2], Hiroyuki Takatsu[2,3], Yohei Katoh[2], Ayako Hanai[2], Tomoko Ueda[2], Yasunori Kanaho[4], Yong Xie[5], Hye-Won Shin[2,3], Hironari Kamikubo[6], Mikio Kataoka[6], Masato Kawasaki[1], Ryuichi Kato[1], Soichi Wakatsuki[1,†] and Kazuhisa Nakayama[2,†]**

[1] Structural Biology Research Center, Photon Factory, Institute of Materials Structure Science, High Energy Accelerator Research Organization (KEK), Tsukuba, Ibaraki 305-0801, Japan; [2]Graduate School of Pharmaceutical Sciences and [3] Career-Path Promotion Unit for Young Life Scientists, Kyoto University, Sakyo-ku, Kyoto 606-8501, Japan; [4] Graduate School of Comprehensive Human Sciences and Institute of Basic Medical Sciences, University of Tsukuba, Tsukuba 305–8575, Japan; [5]Institute of Medicinal Plant Development, Chinese Academy of Medical Sciences and Peking Union Medical College, Haidian District, Beijing 100193, China; and [6]Graduate School of Materials Science, Nara Institute of Science and Technology, Ikoma, Nara 630-0192, Japan

**Supplementary Materials and Methods**

***Reagents and antibodies***

Polyclonal rabbit anti-Arf6 antibody was raised as described previously (Akiyama et al, 2010). Sources of other antibodies and reagents were: monoclonal mouse anti-Arf6 (3A-1) and anti-MgcRacGAP (A-6) and polyclonal rabbit anti-MKLP1 (N-19), Santa Cruz Biotechnology; monoclonal rat anti-α-tubulin, Abcam; monoclonal mouse anti-β-tubulin (KMX-1), Chemicon; monoclonal rat anti-HA (3F10), Roche Applied Science; AlexaFluor-conjugated secondary antibodies and SYTOX Green, Molecular Probes.

***Plasmids***

Human Arf cDNA was cloned into the pcDNA3-HAC (Hosaka et al, 1996), pEGFP-N3 (Invitrogen), or pcDNA3-mCherry vector constructed from an mCherry vector originally provided by Roger Tsien (Shaner et al, 2005). Human MKLP1 cDNA was cloned into pcDNA3-mRFP provided by Roger Tsien or pCAG-HAN, which is derived from pCAGGS (Niwa et al, 1999). Truncated forms of the MKLP1 cDNA and a cDNA fragment for human JIP4-LZII (Isabet et al, 2009) were generated by PCR and cloned into pGEX4T-2 (GE Healthcare). Mutations were introduced into the Arf6 and MKLP1 cDNAs using a QuikChange Lightning Site-Directed Mutagenesis kit (Agilent Technologies). Expression vectors for GST-fused GGA1-GAT, GGA2-GAT and FIP4(484-613) were constructed as described previously (Shiba et al, 2006; Takatsu et al, 2002).

***Protein expression and purification***

Human MKLP1 (690–807) (cMKLP1) and mouse Arf6(Q67L, 13–175) were cloned into pGEX-4T-2 and pET28a (Merck KGaA), respectively. GST-cMKLP1 and Arf6(Q67L)-His6 were co-expressed in *E. coli* BL21(DE3) cells at 20°C overnight. The expressed cMKLP1 protein is sensitive to proteases (Figure S4). Selenomethionine (Se-Met)-labeled GST-cMKLP and Arf6(Q67L)-His6 were co-expressed in LeMaster medium containing Se-Met (Wako Pure Chemical). Cells were disrupted by sonication in Buffer A (20 mM Tris-HCl pH 7.6, 5 mM $MgCl_2$, 5 mM 2-mercaptoethanol) containing 300 mM NaCl and protease inhibitor cocktail (Roche Applied Science). After centrifugation, the supernatant was applied to a glutathione-Sepharose 4B column, and the GST-tag was cleaved off using thrombin (GE Healthcare) at 20°C overnight. The eluate was passed through benzamidine-Sepharose 4FF (GE Healthcare) and glutathione-Sepharose 4B columns. Finally, the Arf6–cMKLP1 complex was isolated by Superdex 75 column (GE Healthcare) with Buffer A containing 200 mM NaCl.

***SPR measurements***

C-terminally His6-tagged Arf1(Q71L, 18-181), Arf3(Q71L, 18-181) and Arf5(Q71L, 18-181) were expressed in *E. coli* BL21(DE3) cells and purified as described above for Arf6(Q67L,

13-175)-His6. SPR measurements were performed using a BIAcore2000 (GE Healthcare). GST-cMKLP1 was captured on a CM5 sensor chip using GST capture kit (GE Healthcare). Binding of Arf1, Arf3, Arf5 or Arf6 to GST-cMKLP1 was analyzed at a flow rate of 20 µl $min^{-1}$ at 25°C in 10 mM HEPES, pH 7.5, 300 mM NaCl, 5 mM $MgCl_2$ and 0.005 % Surfactant P20. The sensorgram was analyzed using the BIAevaluation 3.2 software. $K_d$ values were determined using the steady-state affinity model by plotting resonance ($R_{eq}$) levels against protein concentrations.

## Supplementary Figures

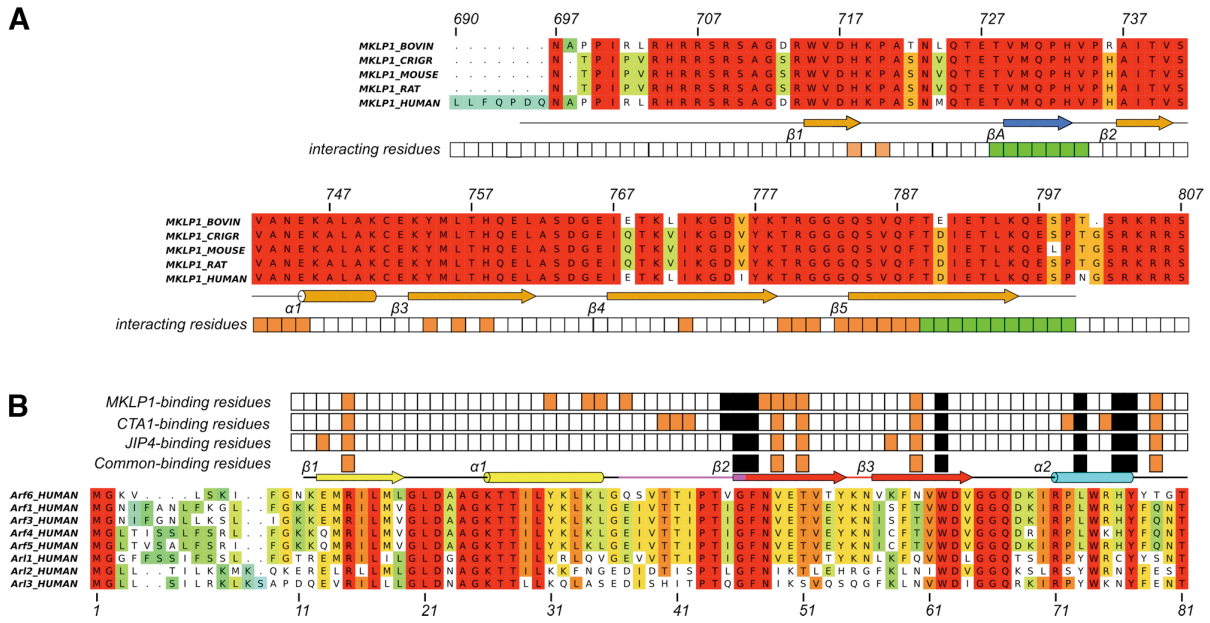


**Figure S1. Multiple alignments and interacting residues of MKLP1 and Arf6**

(A) Alignment of mammalian MKLP1 (KIF23) sequences. From bottom to top, aligned amino acid sequences of the cMKLP1 region of *Homo sapiens* (human), *Rattus norvegicus* (rat), *Mus musculus* (mouse), *Cricetulus griseus* (Chinese hamster) and *Bos taurus* (bovine). The numbers correspond to residue numbers of human MKLP1 (residues 690–807). Alignment was performed with PROBCONS (Do et al, 2005) and colored by ALINE (Bond & Schuttelkopf, 2009). Degrees of sequence similarity are colored from cyan to red (with low similarity cutoff = 0) in ALINE. Secondary structure was assigned by DSSP (Kabsch & Sander, 1983) and is colored in orange. The βA region colored in royal blue constitutes a small β sheet in the homodimer, but might be a part of a loop in the monomer. The residues involved in Arf6 binding and in cMKLP1 binding on cMKLP1 dimer interface are represented as tiles colored in orange and green, respectively. (B) Alignment of sequences of human Arf and Arl proteins. From top to bottom, aligned acid sequences of Arf6, Arf1, Arf3, Arf4, Arf5, Arl1, Arl2 and Arl3. The numbers correspond to residue numbers of Arf6 (residues 1–81). Alignment, coloring of similarity and secondary structure assignment were generated using the same software as in (A). Secondary structures of Arf6 are colored with purple (Sw1), red (interswitch), cyan (Sw2) and yellow (other regions). The Arf6 residues involved in binding to cMKLP1, CTA1 (PDB 2A5D) or JIP4 (PDB 2W83) are represented as tiles in row above the secondary structure. The residues of Arf6 commonly used for binding to three effector proteins (cMKLP1, CTA1 and JIP4) are also represented as tiles. The orange and black tiles specify residues involved in effector binding and the effector-binding patch (O'Neal et al, 2005), respectively.

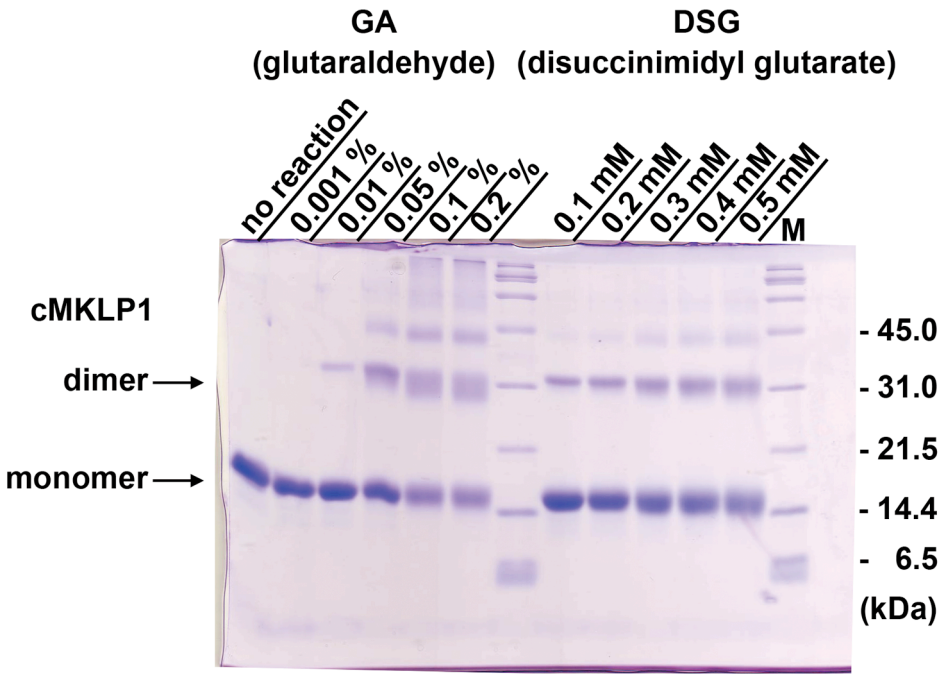


**Figure S2. Chemical cross-linking of MKLP1**

cMKLP1 was expressed and purified by the same procedures used for the Arf6–cMKLP1 complex. cMKLP1 was dissolved at a concentration of 1.0 mg/ml in 50 mM sodium phosphate, pH 7.4, 300 mM NaCl and subjected to cross-linking using glutaraldehyde (GA) or disuccinimidyl glutarate (DSG). 1 µl of GA or DSG solution in dimethylformamide was added to 9 µl of the protein solution, yielding final concentrations of 0.01–2% or 1–5 mM, respectively. After incubation for 60 min on ice, the unreacted cross-linking reagent was quenched by the addition of 1 M Tris-HCl, pH 7.4. The cross-linked proteins were analyzed by 17.5% (w/v) SDS–PAGE.

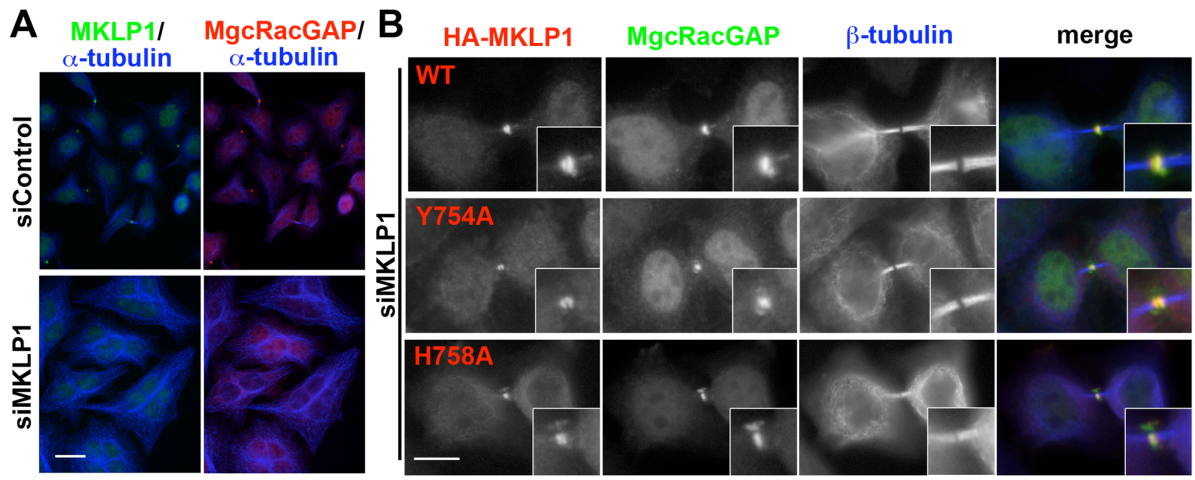


**Figure S3. Recovery of MgcRacGAP localization to the Flemming body by exogenous expression of wild-type and mutant MKLP1 in MKLP1 siRNA-treated cells**

(A) MKLP1 depletion abolishes MgcRacGAP/Cyk4 localization to the Flemming body. HeLa cells treated with a pool of siRNAs for LacZ (siControl) or MKLP1 were triply immunostained for MKLP1 (green), MgcRacGAP (red), and β-tubulin (blue). Note that a number of the control cells exhibit both the MKLP1 and MgcRacGAP signals on the Flemming body or its remnant. (B) HeLa cells were transfected with an expression vector for HA-MKLP1(WT), HA-MKLP1(Y754A), or HA-MKLP1(H758A), together with siRNAs for MKLP1. After 48 hr, the cells were fixed and triply immunostained for HA, MgcRacGAP and β-tubulin. Bars, 10 μm.

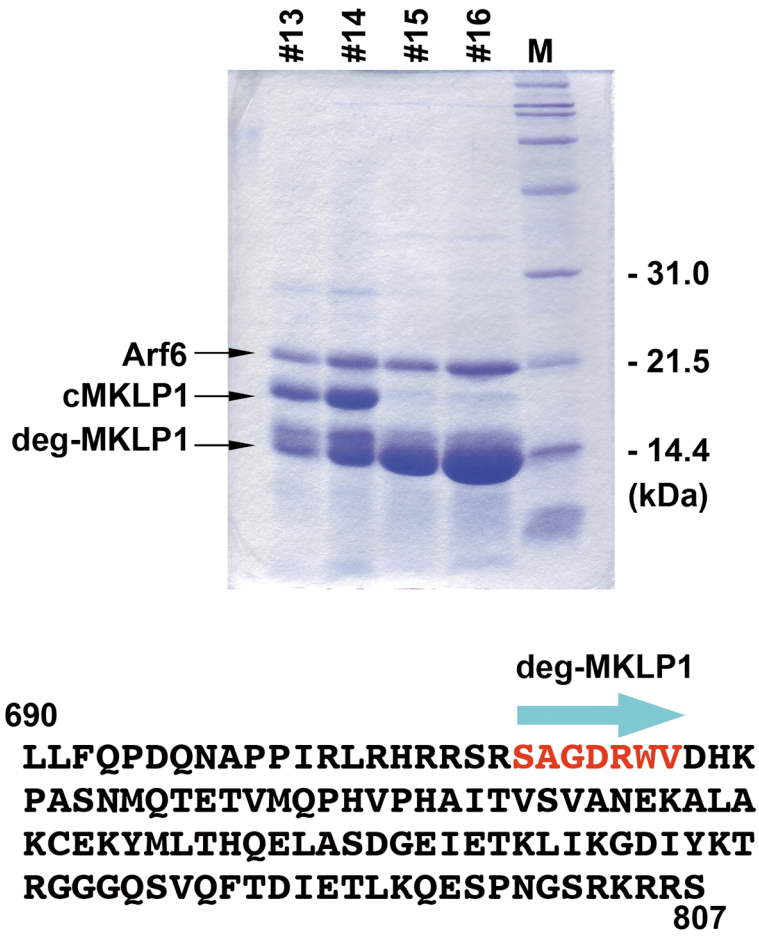


**Figure S4. Protease sensitive region of cMKLP1**

SDS–PAGE analysis of the major peak fractions from gel-filtration (Superdex 75) before optimizing purification of the Arf6–cMKLP1 complex (upper panel). The determined N-terminal sequence of the degraded cMKLP1 product (deg-MKLP1) was $^{710}$SAGDRWV (lower panel, colored in red).

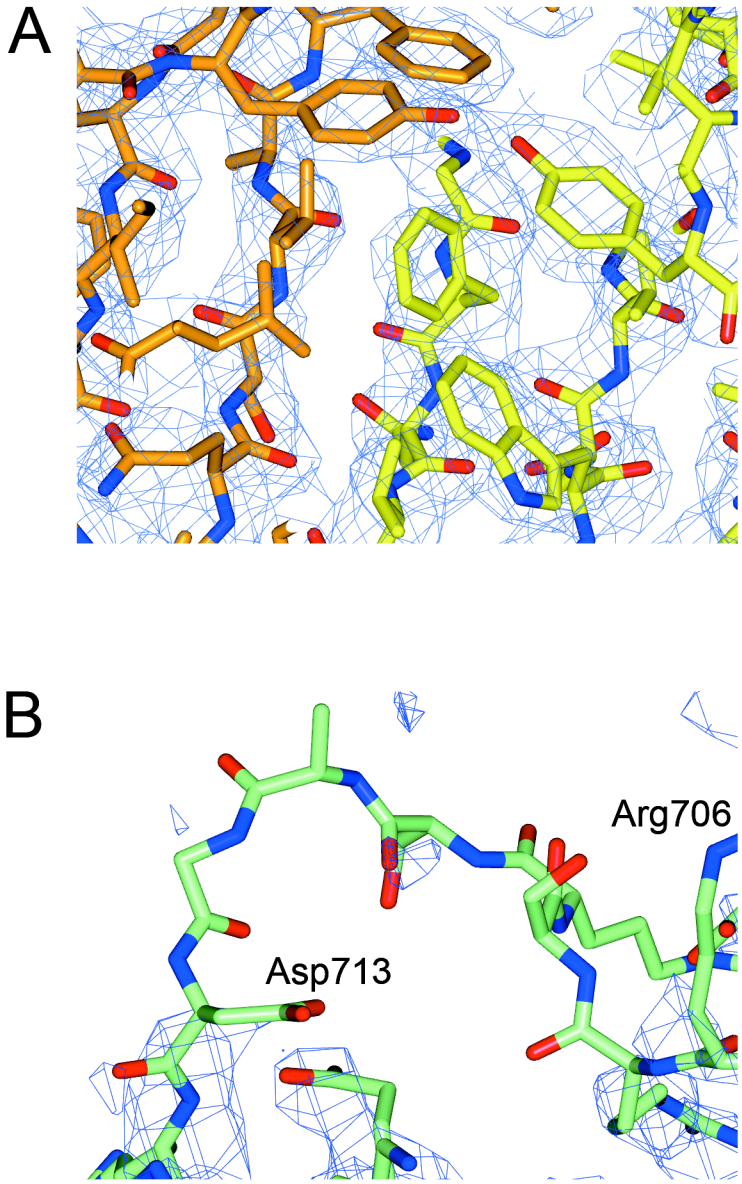


**Figure S5. The simulated annealing omit map of the Arf6–cMKLP1 complex and the omit region of MKLP1**

**(**A) The simulated annealing omit map (omit region is between Arg706 and Asp713 on cMKLP1) of the Arf6–cMKLP1 complex at 3.0 Å resolution. The map is contoured at 1.0 σ by CCP4MG (Potterton et al, 2004); Arf6 and cMKLP1 are represented as yellow and orange sticks, respectively. (B) The omit region of cMKLP1 from Arg706 to Asp713. The simulated annealing omit map is shown with the stick representation of cMKLP1. Although the working and free R factors were refined to 19.0% and 22.1%, respectively (Figure S6A and Table S2), only two cMKLP1 molecules have clear electron density between Asp695 to Arg707 in 2*m*Fo-*D*Fc map. In the third cMKLP1 molecule, there was a low electron-density region from Asp695 to Ala698. Likewise, we could not

model the fourth cMKLP1 molecule due to a low electron-density region from Asp695 to Gly712. None of the four cMKLP1 molecules showed clear electron-density in the region from Arg707 to Gly712 during refinement of the electron-density map. Because the region corresponds to the protease-sensitive region (Figure S5), it may be flexible or susceptible to partial cleavage during the crystallization process.

**Supplementary Tables**

**Table S1. Buried surface area and shape complementary for effector protein and GTPase complex**

PDBePISA (Krissinel & Henrick, 2007) server was used to calculate buried surface area. The shape complementarity of two interacting molecular surfaces was determined by SC (Lawrence & Colman, 1993).

| | Buried surface area (Å$^2$) | | | Sc value |
|---|---|---|---|---|
| | Effector | Arf/Arl | Total | |
| cMKLP1:Arf6-GTP (chain A-B) | 1105.8 | 1135.2 | 2241.0 | 0.69 |
| CTA1:Arf6-GTP (PDB 2A5D, chain A-B) | 911.0 | 1003.6 | 1914.6 | 0.72 |
| JIP4-LZII:Arf6-GTP (PDB 2W83, chain A-C-D) | 843.0 (386.7+456.3) | 815.2 (379.2+436.0) | 1658.2 | 0.78 |
| 2002 PDE:Arl2-GTP (PDB 1KSH, chain A-B) | 788.7 | 809.6 | 1598.3 | 0.71 |
| 2003 GRIP:Arl1-GTP (PDB 1UPT, chain A-B) | 644.0 | 652.3 | 1296.3 | 0.66 |
| 2003 GGA1GAT:Arf1-GTP (PDB 1J2J, chain A-B) | 588.9 | 619.2 | 1208.1 | 0.70 |
| | cMKLP1 | cMKLP1 | | |
| cMKLP1:cMKLP1 (chain B-D) | 1035.1 | 1045.3 | 2080.4 | 0.78 |

**Table S2. Data collection and refinement statistics**

Highest resolution shell is shown in parentheses. Numbers in parentheses indicate values for the highest resolution shell. I/σ is the mean reflection intensity divided by the average estimated error.

| **Dataset** | Native (AR-NW12A) | Se-Met (BL-5A) |
|---|---|---|
| **Data collection** | | |
| Space Group | $P2_1$ | $P2_1$ |
| Cell dimensions | | |
| a, b, c (Å) | 45.7, 174.6, 76.8 | 40.8, 173.2, 45.9 |
| α, β, γ (°) | 90.0, 98.7, 90.0 | 90.0, 111.4, 90.0 |
| Wavelength (Å) | 1.0000 | 0.9788 |
| Resolution (Å) | 50.00-2.80 | 50.00-2.54 |
| Rmerge | 0.115 (0.837) | 0.098 (0.414) |
| I/σ | 15.4 (1.7) | 13.6 (2.2) |
| Completeness (%) | 99.9 (99.6) | 90.1 (86.7) |
| Redundancy | 4.2 (3.9) | 2.9 (2.3) |
| **Refinement** | | |
| Resolution (Å) | 30.00-3.0 | 50.00-2.54 |
| No. reflections | 22575 | 16599 |
| $R_{work}$ / $R_{free}$ | 0.190/0.221 | 0.235/0.282 |
| No. atoms | | |
| Protein | 8486 | 4273 |
| Water | 105 | |
| B-factors | | |
| Protein (average) | 55.0 | 43.1 |
| Arf6 | 55.7 | |
| cMKLP1 | 54.4 | |
| water | 45.2 | |
| R.m.s deviation | | |
| Bond length (Å) | 0.008 | 0.010 |
| Bond angles (°) | 1.076 | 1.413 |
| Ramachandran plot | | |
| Favored (%) | 98.2 | 97.2 |
| Allowed (%) | 1.8 | 2.4 |

**Supplementary Movie Legends**

**Movie S1. Spatiotemporal changes in the localization of Arf6-EGFP during cell division**

HeLa cells transfected with an expression vector for Arf6-EGFP were subjected to three-dimensional time-lapse recording. Left and right movies, rotated by 90° with respect to the z axis, show the same two cells (indicated by yellow and magenta asterisks in Figure 1C). Images were collected sequentially every 5 min; the video frame rate is 12 frames/sec.

**Movie S2. Three-dimensional image analysis of Arf6-EGFP localization around the cleavage furrow**

HeLa cells expressing Arf6-EGFP were fixed and subjected to three-dimensional image analysis. A representative cell image with Arf6-EGFP signals at the cleavage furrow is shown. Note that the Arf6-EGFP signals appear to be in the cortical region of the cleavage plane, rather than on the central spindle.

**Movie S3. Spatiotemporal changes in the localization of Arf6-EGFP and mRFP-MKLP1 during cell division**

HeLa cells transfected with expression vectors for Arf6-EGFP and mRFP-MKLP1 were subjected to time-lapse recording. Images were collected sequentially every 5 min; the video frame rate is 3 frames/sec. Note that an MKLP1 signal in the lower dividing cell may represent a Flemming body remnant carried over from the previous cell division.

**Supplementary References**

Akiyama M, Zhou M, Sugimoto R, Hongu T, Furuya M, Funakoshi Y, Kato M, Hasegawa H, Kanaho Y (2010) Tissue- and development-dependent expression of the small GTPase Arf6 in mice. *Dev Dyn* **239:** 3416-3435

Bond CS, Schuttelkopf AW (2009) ALINE: a WYSIWYG protein-sequence alignment editor for publication-quality alignments. *Acta Crystallogr D* **65:** 510-512

Do CB, Mahabhashyam MS, Brudno M, Batzoglou S (2005) ProbCons: Probabilistic consistency-based multiple sequence alignment. *Genome Res* **15:** 330-340

Hosaka M, Toda K, Takatsu H, Torii S, Murakami K, Nakayama K (1996) Structure and intracellular localization of mouse ADP-ribosylation factors type 1 to type 6 (ARF1-ARF6). *J Biochem* **120:** 813-819

Isabet T, Montagnac G, Regazzoni K, Raynal B, El Khadali F, England P, Franco M, Chavrier P, Houdusse A, Ménétrey J (2009) The structural basis of Arf effector specificity: the crystal structure of ARF6 in a complex with JIP4. *EMBO J* **28:** 2835-2845

Kabsch W, Sander C (1983) Dictionary of protein secondary structure: pattern recognition of hydrogen-bonded and geometrical features. *Biopolymers* **22:** 2577-2637

Krissinel E, Henrick K (2007) Inference of macromolecular assemblies from crystalline state. *J Mol Biol* **372:** 774-797

Lawrence MC, Colman PM (1993) Shape complementarity at protein/protein interfaces. *J Mol Biol* **234:** 946-950

Niwa H, Yamamura K, Miyazaki J (1999) Efficient selection for high-expression transfectants with a novel eukaryotic vector. *Gene* **108:** 193-200

O'Neal CJ, Jobling MG, Holmes RK, Hol WG (2005) Structural basis for the activation of cholera toxin by human ARF6-GTP. *Science* **309:** 1093-1096

Potterton L, McNicholas S, Krissinel E, Gruber J, Cowtan K, Emsley P, Murshudov GN, Cohen S, Perrakis A, Noble M (2004) Developments in the CCP4 molecular-graphics project. *Acta Crystallogr D* **60:** 2288-2294

Shaner NC, Steinbach PA, Tsien RY (2005) A guide to choosing fluorescent proteins. *Nat Methods* **2:** 905-909

Shiba T, Koga H, Shin H-W, Kawasaki M, Kato R, Nakayama K, Wakatsuki S (2006) Structural basis for Rab11-dependent membrane recruitment of family of Rab11-interacting protein (FIP3)/Arfophilin-1. *Proc Natl Acad Sci USA* **103:** 15416-15421

Takatsu H, Yoshino K, Toda K, Nakayama K (2002) GGA proteins associate with Golgi membranes through interaction between their GGAH domains and ADP-ribosylation factors. *Biochem J* **365:** 369-378